ENGINEERING

Tissue-embedded stretchable nanoelectronics reveal endothelial cell-mediated electrical maturation of human 3D cardiac microtissues

Zuwan Lin¹†, Jessica C. Garbern^{2,3}†‡, Ren Liu⁴†, Qiang Li⁴, Estela Mancheño Juncosa², Hannah L.T. Elwell²§, Morgan Sokol², Junya Aoyama², Undine-Sophie Deumer², Emma Hsiao⁴, Hao Sheng⁴, Richard T. Lee^{2,5}*, Jia Liu⁴*

Clinical translation of stem cell therapies for heart disease requires electrical integration of transplanted cardiomyocytes. Generation of electrically matured human induced pluripotent stem cell-derived cardiomyocytes (hiPSC-CMs) is critical for electrical integration. Here, we found that hiPSC-derived endothelial cells (hiPSC-ECs) promoted the expression of selected maturation markers in hiPSC-CMs. Using tissue-embedded stretchable mesh nanoelectronics, we achieved a long-term stable map of human three-dimensional (3D) cardiac microtissue electrical activity. The results revealed that hiPSC-ECs accelerated the electrical maturation of hiPSC-CMs in 3D cardiac microtissues. Machine learning—based pseudotime trajectory inference of cardiomyocyte electrical signals further revealed the electrical phenotypic transition path during development. Guided by the electrical recording data, single-cell RNA sequencing identified that hiPSC-ECs promoted cardiomyocyte subpopulations with a more mature phenotype, and multiple ligand-receptor interactions were up-regulated between hiPSC-ECs and hiPSC-CMs, revealing a coordinated multifactorial mechanism of hiPSC-CM electrical maturation. Collectively, these findings show that hiPSC-ECs drive hiPSC-CM electrical maturation via multiple intercellular pathways.



INTRODUCTION

Ventricular arrhythmias following delivery of human induced pluripotent stem cell–derived cardiomyocytes (hiPSC-CMs) in large animal models prevent clinical translation of such technologies for the treatment of heart disease (1–3). Immature hiPSC-CMs exhibit automaticity, or spontaneous action potentials, which interferes with conduction patterns of native cells, leading to arrhythmias (1, 2). Within a few weeks after delivery of hiPSC-CMs to infarcted myocardium of macaques or pigs, the propensity for ventricular arrhythmias resolves, presumably due to maturation of the CMs following exposure to the in vivo environment (1, 2). The mechanisms leading to the eventual suppression of CM automaticity remain unclear.

Communication between endothelial cells (ECs) and CMs is important during development (4, 5). For example, neuregulin (NRG) is secreted by ECs during early development to direct CM phenotype away from a nodal subtype (6) and promote cardiac trabeculation via ErbB receptor signaling (7). In addition, EC-specific deletion of platelet-derived growth factor B can lead to myocardial thinning and chamber dilation (8). We previously demonstrated that microvascular ECs could promote murine neonatal CM

survival and spatial organization (9), and coculture of ECs with PSC-CMs has previously been shown to improve certain aspects of PSC-CM maturation (10). Specifically, coculture of PSC-ECs with PSC-derived cardiac progenitor cells accelerated the maturation of PSC-CMs with increased expression of TNNT2, MLC2v, MYH7, KCNJ2, and ATP2A2, increased CM size, and an enhanced chronotropic response to isoprenaline (10). Similarly, PSC-CMs cocultured with PSC-ECs with or without amniotic mesenchymal stem cells increase the expression of CACNA1C and KCNJ2 (11). There is a cross-talk effect as PSC-ECs in coculture with PSC-CMs acquire a cardiac EC phenotype, supporting a synergistic role for CM/EC coculture (12). Cotransplantation of microvessels with hiPSC-CMs in infarcted rat hearts also improves hiPSC-CM survival and maturation (13). When implanted as a patch onto uninjured myocardium in mice, human blood-derived endothelial colony-forming cells enhance the survival and engraftment of PSC-CMs, and this effect is attributed at least in part to the secretion of NRG1 from ECs (14). While these prior studies demonstrate that ECs can promote a more mature CM phenotype, the mechanisms by which ECs influence the electrical phenotype of hiPSC-CMs remain unclear. Here, we integrated tissue-embedded stretchable electronics for real-time electrophysiology with machine learning (ML)-based algorithms for high-dimensional electrical recording data and revealed an accelerated electrical maturation of hiPSC-CMs by coculturing with hiPSC-ECs. This paradigm for real-time electrophysiology and data analysis will readily be applied to investigate the electrical maturation across different types of stem cellderived cardiac tissues and protocols.

Existing methods to assess three-dimensional (3D) cardiac microtissue functional maturation either lack single-cell resolution across the intact tissue network or cannot simultaneously measure

¹Department of Chemistry and Chemical Biology, Harvard University, Cambridge, MA, USA. ²Department of Stem Cell and Regenerative Biology, Harvard University, Cambridge, MA, USA. ³Department of Cardiology, Boston Children's Hospital, Boston, MA, USA. ⁴School of Engineering and Applied Sciences, Harvard University, Boston, MA, USA. ⁵Division of Cardiovascular Medicine, Department of Medicine, Brigham and Women's Hospital, Boston, MA, USA.

[†]These authors contributed equally to this work.

[‡]Present address: Vertex Pharmaceuticals, Boston, MA, 02210, USA.

[§]Present address: Graduate School of Biomedical Sciences and Tufts University School of Medicine, Tufts University, Boston, MA 02111, USA.

^{*}Corresponding author. Email: jia_liu@seas.harvard.edu (J.L.), richard_lee@ harvard.edu (R.T.L.)

tissue-wide activities of individual cells in a chronically stable manner over the time course of their maturation. Imaging-based detection of Ca²⁺ activity depends on transient stains, which are incompatible with long-term stable measurements and only provide indirect measurements of cell electrophysiology (15). Intracellular electrophysiology recordings such as patch clamp can only assay cells one at a time, require membrane disruption, locally singularize spatially distributed electrical activities, and are challenging for 3D cardiac microtissue application (16-19). Extracellular recordings such as classic multielectrode arrays are noninvasive and offer high spatiotemporal resolution but contact cardiac microtissues only at one plane in their surface and lose contact quickly due to the mechanical contraction (17, 20). The development of "tissuelike" electronics (21-27) through the convergence of soft and flexible materials and nanoelectronics incorporates tissue-like properties such as tissue-level flexibility, subcellular feature size, and meshlike networks (28–30) into nanoelectronics, allowing for seamlessly integrating electronics throughout 3D tissue and stably recording cell electrophysiology at single-cell resolution (31-34). Notably, we recently further advanced methods for implanting and distributing nanoelectronics across entire microtissue bodies. The tissueembedded electronics enable chronic, tissue-wide, 3D electrophysiology recordings throughout organogenesis with minimal impact on growth and differentiation (32, 33). Here, we used this system to characterize the electrical maturation of 3D hiPSC-CM microtissues with or without hiPSC-derived ECs (hiPSC-ECs). Specifically, this study revealed that human hiPSC-ECs can enhance the electrical maturation of human hiPSC-CMs in vitro. The long-term stable electrical mapping revealed substantial electrical maturation and coordination of hiPSC-CMs by hiPSC-ECs. We applied the pseudotime trajectory inference, an ML-based approach, to analyze the high-dimensional electrical waveforms continuously recorded from the same 3D cardiac microtissues, reconstructing and illustrating the continuous phenotypic evolution path and accelerated electrical maturation level. Then, we used single-cell RNA sequencing (scRNA-seq) to analyze the maturation stage identified by the electrical recording. Combining electrical recording results with singlecell gene expression profiling, the results further elucidated potential mechanisms of how ECs promote electrical maturation of hiPSC-CMs. Collectively, the multimodal single-cell analysis demonstrated the coordination of multiple intercellular communication pathways that drive the molecular events for the observed EC-mediated CM electrical maturation.

RESULTS

hiPSC-ECs enhance the expression of CM maturation markers in hiPSC-CMs

We differentiated hiPSCs into either CMs or ECs using protocols adapted from prior publications (Fig. 1, A and B) (35, 36). We cocultured hiPSC-CMs with or without hiPSC-ECs at different CM:EC seeding ratios for 7 days and then performed flow cytometry to evaluate the expression of selected markers of CM maturation (Fig. 1, C and D). Final percentages of hiPSC-CMs (identified as TNNT2⁺ cells) and hiPSC-ECs (identified as CD144⁺ cells) are shown in Fig. 1E. We found that hiPSC-ECs increased the percentage of TNNT2⁺ hiPSC-CMs expressing TNNI3, inwardly rectifying potassium channel 2.1 (Kir2.1), connexin 43 (Cx43), and CD36, in a dose-dependent manner (Fig. 1F). In addition, the mean

fluorescence intensity (MFI) of TNNT2, TNNI3, Kir2.1, Cx43, and CD36 increased in hiPSC-CMs cultured with hiPSC-ECs compared to hiPSC-CMs cultured alone (Fig. 1, G to K). TNNT2 and TNNI3 showed similar increases in MFI at 1:1, 2:1, or 3:1 CM:EC ratios compared to 4:1 or hiPSC-CMs alone (Fig. 1, G and H). Cx43 and CD36 showed the highest levels with a 3:1 CM:EC ratio, and Kir2.1 showed the highest levels with a 1:1 CM:EC ratio (Fig. 1, I to K). Subsequent experiments used a 3:1 CM:EC seeding ratio given that this ratio provided increased gene expression of the most genes out of the genes selected for initial screening.

hiPSC-ECs promote hiPSC-CM electrical and sarcomere maturation

We seeded hiPSC-CMs with or without hiPSC-ECs onto stretchable mesh nanoelectronics/Matrigel hybrid structures for long-term electrical recording (Fig. 2A and fig. S1A). Stretchable mesh nanoelectronics were fabricated as per our previously reported protocol (32, 33). Specifically, microelectrodes were patterned in the 1-µmthick serpentine stretchable interconnects with the central region formed by straight interconnects. The straight lines in the center region could better maintain the overall geometry of the stretchable mesh nanoelectronics after releasing from the substrate. Meanwhile, the wave-like interconnect structures between the center region and input/output (I/O) connectors can provide the initial stretchability to accommodate the cardiac contraction. In addition, after stem cell growth, the initial cell sheet will shrink into a cell plate due to the cell-cell interactions, which resulted in buckling of the straight lines in the central region of the stretchable mesh nanoelectronics, allowing the entire device to become stretchable. This design ensures tissue-level bending stiffness and accommodates the 3D morphological change of the tissue throughout the development and contraction of the CMs for stable electrical recording. We validated the long-term performance of the stretchable mesh nanoelectronics in physiological conditions. The electrodes maintained chronically stable, highly uniform, low impedance across multiple devices over 7 weeks, demonstrating performance stability to characterize the change of cellular signals from the same sample during longterm, continuous measurement (fig. S2). Before culture, stretchable mesh nanoelectronics were released from the fabrication substrate. A thin layer of Matrigel was cured underneath the freestanding stretchable mesh nanoelectronics. Cells were seeded on the top of the electronics/Matrigel hybrid. Over the course of development, cells seamlessly integrated with the electronics/Matrigel hybrid, forming 3D cardiac patches. This seamlessly integrated tissue/electronics structure allows intimate coupling between cells and electrodes, enabling long-term stable, continuous, and high signal-tonoise ratio recording at the cellular level (Fig. 2A).

Samples cocultured with both hiPSC-CMs and hiPSC-ECs were prepared at a 3:1 CM:EC seeding ratio (hiPSC-CMs seeded on day 11 of differentiation; hiPSC-ECs seeded on day 14 of EC differentiation). As an example, we acquired raw voltage tracings and extracted channel-averaged extracellular field potential spike waveforms from samples at day 37 of hiPSC-CM differentiation (day 26 after initiation of hiPSC-CM + hiPSC-EC coculture) (representative images from 16 channels per sample group depicted in Fig. 2B). Electrical signals between each channel show obvious time delay, demonstrating the ability of tissue-wide distributed electrodes to record the signals from different CMs in 3D hiPSC-CM tissues instead of recording the same CM signals by multiple electrodes

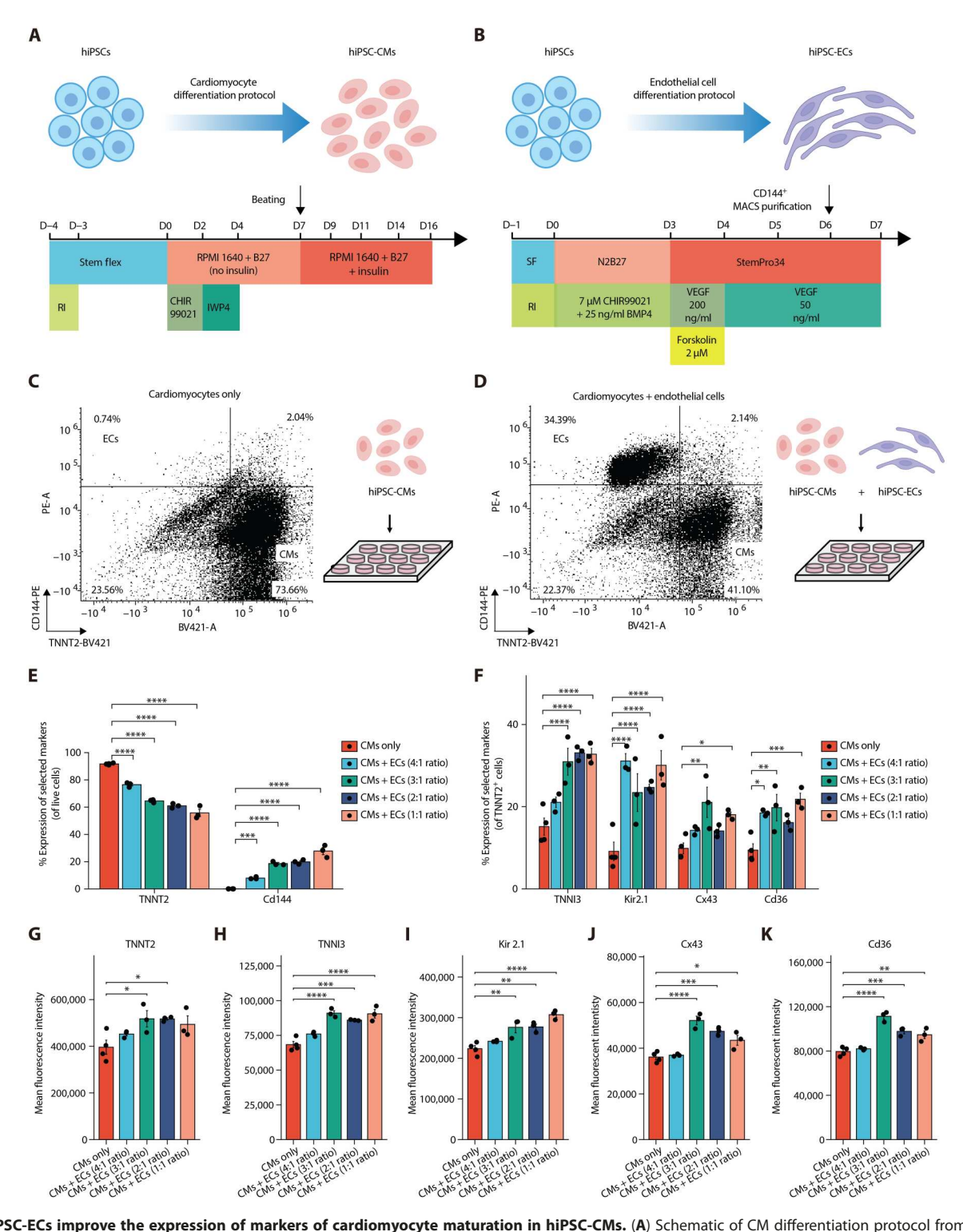


Fig. 1. HiPSC-ECs improve the expression of markers of cardiomyocyte maturation in hiPSC-CMs. (A) Schematic of CM differentiation protocol from hiPSCs. (B) Schematic of EC differentiation protocol from hiPSCs. MACS, magnetic-activated cell sorting; VEGF, vascular endothelial growth factor. (C) Sample flow cytometry dot plot showing gating strategy for population of TNNT2+ hiPSC-CMs or (D) TNNT2+ hiPSC-CMs cocultured with CD144+ hiPSC-ECs. PE-A, phycoerythrin-area. (E) Percent expression of TNNT2 or CD144 in live cells with different seeding ratios of CMs:ECs. ***P < 0.001 and ****P < 0.0001 by two-way analysis of variance (ANOVA) with Dunnett's multiple comparisons test. (F) Percent expression of TNNI3, Kir2.1, Cx43, or Cd36 in TNNT2+ hiPSC-CMs with different seeding ratios of CMs:ECs. *P < 0.05, **P < 0.01, ***P < 0.001, and ****P < 0.0001 by two-way ANOVA with Dunnett's multiple comparisons test. (G to K) Mean fluorescence intensity (MFI) of (G) TNNT2-BV421, (H) TNNI3-AS647, (I) Kir2.1-FITC, (J) Connexin 43-AF750, and (K) Cd36-AF594. *P < 0.05, **P < 0.05, **P < 0.001, and ****P < 0.0001 by one-way ANOVA with Dunnett's multiple comparisons test.

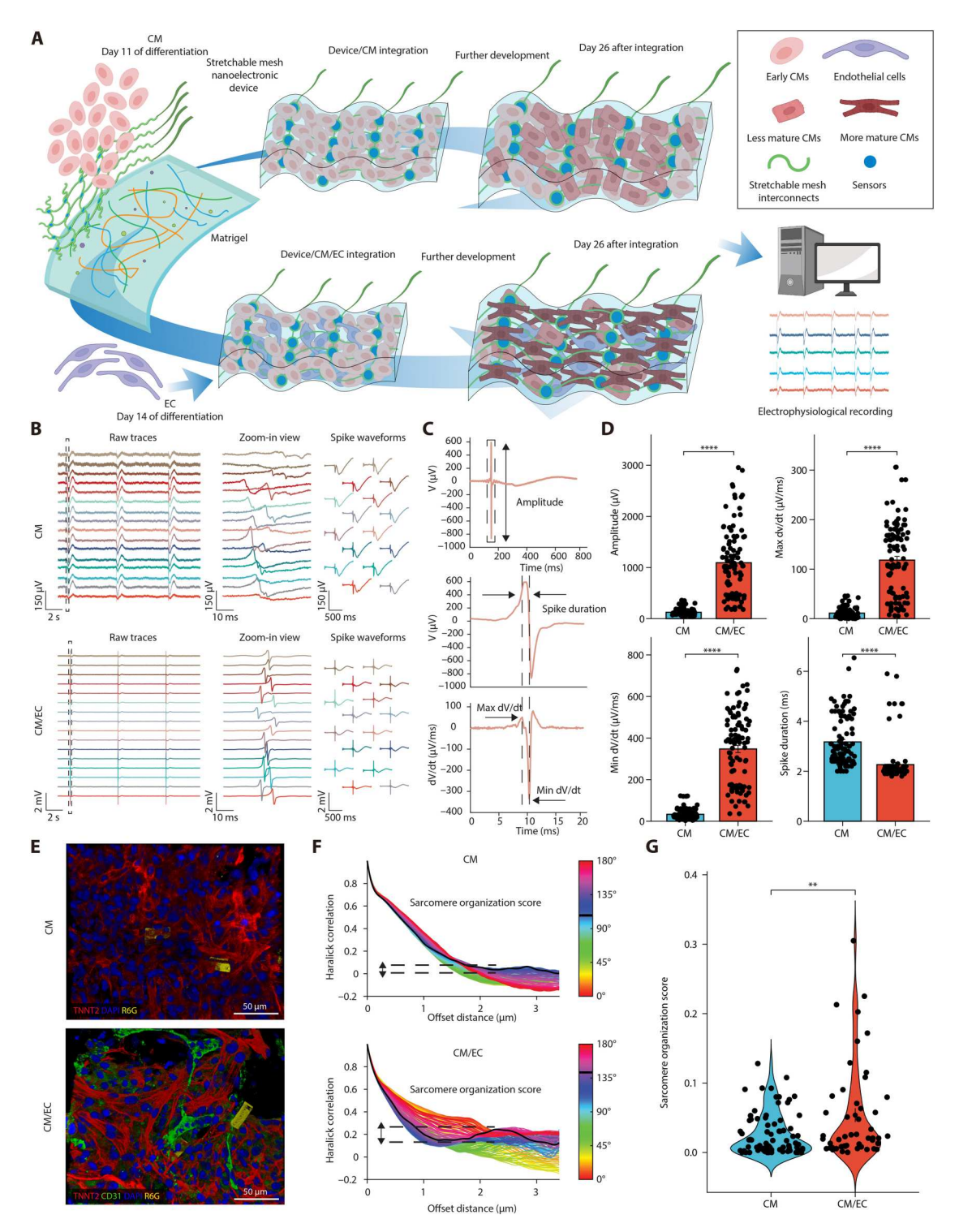


Fig. 2. HiPSC-ECs improve the electrical and structural maturation of hiPSC-CM differentiation. (**A**) Schematics of hiPSC-CMs and hiPSC-CMs/hiPSC-EC coculture integrating with stretchable mesh nanoelectronics for long-term stable electrical measurement. (**B**) Representative raw voltage traces, zoom-in traces, and extracted channel-averaged spike waveforms showing extracellular electrical activities at day 37 of hiPSC-CMs differentiation (day 26 of coculture) for hiPSC-CMs (top) and hiPSC-CMs/hiPSC-ECs (bottom). (**C**) Schematics showing the definition of electrical features from spike waveforms for analysis. (**D**) Comparison of spike waveform features of hiPSC-CMs and hiPSC-CMs/hiPSC-ECs at day 37 of differentiation. Data are means \pm SEM; *****P < 0.0001 by two-tailed, unpaired t test. Each dot represents a channel that has electrical signals from eight groups of samples. (**E**) Representative 3D reconstructed fluorescence images showing the sarcomere structures in hiPSC-CMs (top) and hiPSC-CMs/hiPSC-ECs (bottom). Red colors correspond to TNNT2; green colors correspond to CD31; blue colors correspond to 4',6-diamidino-2-phenylindole; yellow colors correspond to Rhodamine 6G (R6G) (E-barcodes of nanoelectronics were labeled by R6G). (**F** and **G**) Haralick correlation plots in hiPSC-CMs and hiPSC-CMs/hiPSC-ECs (F) and sarcomere organization score in hiPSC-CMs and hiPSC-CMs/hiPSC-EC coculture (G). Each dot represents a segmented cell from three samples. **P < 0.01 by two-tailed, unpaired t test.

(Fig. 2B). We quantified voltage amplitude, spike duration, maximum dV/dt, and minimum dV/dt from these recordings (Fig. 2C). Comparing hiPSC-CMs to hiPSC-CM/hiPSC-EC samples, statistical analysis showed a significant increase in the voltage amplitude, maximum dV/dt, and minimum dV/dt, and a significant decrease in spike duration (Fig. 2D). We then further compared the recordings from the CMs next to and far away from ECs in the hiPSC-CM/hiPSC-EC samples, and the results showed that CMs next to ECs have higher voltage amplitude, maximum dV/dt, and minimum dV/dt, and a lower spike duration compared to those far away from ECs, suggesting a more mature electrical phenotype in CMs next to ECs (fig. S3). After monthlong continuous recording, we performed fluorescent imaging in the tissue/electronics hybrid. The fluorescence image showed that ECs tend to aggregate in clusters surrounded by CMs and form blood microvessel-like structures within the 3D structures (Fig. 2E). Sarcomere structural analysis by the previously established Haralick method (37) showed a significant improvement in sarcomere alignment in hiPSC-CMs/hiPSC-ECs compared to hiPSC-CMs cultured alone (Fig. 2, E to G).

hiPSC-ECs accelerate electrical maturation of hiPSC-CMs

We then asked how hiPSC-EC coculture accelerated the electrical maturation of hiPSC-CMs over the entire time course of development. We recorded the electrical signals of the same samples at multiple time points over the course of development (days 15, 18, 23, 30, and 37 of hiPSC-CMs differentiation, which is equivalent to days 4, 7, 12, 19, and 26 after reseeding and initiation of coculture) (Fig. 3A). We extracted the extracellular field potential from each channel. The channel-averaged spike waveforms showed more uniform and mature electrical patterns at earlier time points in hiPSC-CMs/hiPSC-ECs compared to hiPSC-CMs cultured alone (Fig. 3B and fig. S4) and revealed an obvious temporal evolution of the electrical activity for both conditions. Statistical analysis further illustrated that the voltage amplitude, maximum dV/dt, and minimum dV/dt were significantly higher, while the spike duration was significantly lower at each time point in hiPSC-CMs/ hiPSC-ECs compared to hiPSC-CMs cultured alone (Fig. 3, C to F). We also observed the evident activation time delay of the spike activities across different channels (fig. S4), which is consistent with previous reports of hPSC-CM electrophysiological recording (21, 31, 38-40). In addition, the tissue-level flexibility and high stretchability of our mesh design enable seamlessly integrating electronics throughout the entire time course of hPSC-CM tissue development, providing long-term stable electrophysiological recordings, while other methods are typically limited in recording duration because of the limited device stretchability and flexibility so that the device typically contacts with tissue at only one surface plane and will lose contact with tissue due to the mechanical contraction and tissue development (table S1) (21, 31, 38-43). We next further investigated how the activation time delay across different channels changed over the time course of development for both hiPSC-CMs and hiPSC-CMs/hiPSC-ECs (fig. S5). The results show that activation time delays among different channels gradually decreased over the course of development (fig. S5B), which suggests increased electrical coordination among cells in a growing network. Furthermore, statistical analysis illustrated that the maximum activation time delay was significantly reduced at each time point in hiPSC-CMs/ hiPSC-ECs compared to hiPSC-CMs, particularly in earlier time

points. These results further support that hiPSC-ECs could accelerate the electrical coordination of hiPSC-CMs during development (fig. S5B).

The continuous electrical mapping provides unique opportunities for studying the dynamic change in cardiac electrical phenotype; however, quantifying the dynamic evolution of electrical activity remains challenging due to the large cross- and withinsample variations of cell functional states. In this regard, only using few extracted electrical features (e.g., amplitude, spike duration, etc.) to quantify the electrical maturation of CMs is limiting. To address these challenges, we used the previously developed MLbased pseudotime trajectory inference method (44) to analyze the chronic electrical recordings, analyzing the entire waveforms of extracellular field potential and aligning the cardiac electrical activities at different developmental stages and across different samples. Pseudotime trajectory inference methods (44) are frequently used to reconstruct cell developmental trajectory from single-cell transcriptomics data based on unsupervised ML for trajectory topology inference, computationally ordering individual cells according to their progression along the learned developmental trajectory. Therefore, we reasoned that pseudotime trajectory inference methods could also be applied to high-dimensional electrical data from different samples to reconstruct electrophysiological development trajectories and visualize the electrical phenotypic transition paths across different time points of development, quantitatively analyzing and comparing samples from different differentiation conditions.

To achieve accurate functional phenotypic trajectory inference, we first used PHATE (45), an unsupervised nonlinear dimensionality reduction method initially applied to single-cell transcriptomics. Rather than transcriptomics data, we applied PHATE to the highdimensional electrical waveforms generated by our mesh nanoelectronics device. This tool captured both local and global nonlinear structures of the waveforms by projecting the high-dimensional electrical waveforms into a 2D space using an information-geometric distance between data points that efficiently preserved high-dimensional topology. We next used Slingshot (46), a method to identify biological signals for one or more branching trajectories, to perform pseudotime trajectory inference in the PHATE embedding space (Fig. 4A). Using this combined computational approach, we projected long-term electrical recording data from hiPSC-CMs and hiPSC-CM/hiPSC-EC coculture samples to construct an inferred joint pseudotime trajectory that maps the electrical phenotypic transition over the course of cardiac development (Fig. 4B and fig. S6).

We next examined whether the inferred trajectory could accurately capture the change of electrical features at different developmental stages. We mapped electrical features extracted at different developmental stages to their corresponding pseudotime. The results showed the increase of the waveform amplitude, maximum dV/dt, and minimum dV/dt and the decrease of the spike duration along the inferred trajectory, validating that the inferred pseudotime trajectory depicts the extracted electrical feature dynamics (Fig. 4, C to F). We then further examined the trajectory formed by hiPSC-CMs and hiPSC-CMs/hiPSC-ECs. Notably, we observed that, first, hiPSC-CMs and hiPSC-CMs/hiPSC-ECs showed different occupations along the trajectory. Specifically, data from hiPSC-CM samples distributed from the beginning to the middle parts of the trajectory, while data from hiPSC-CM/hiPSC-EC samples

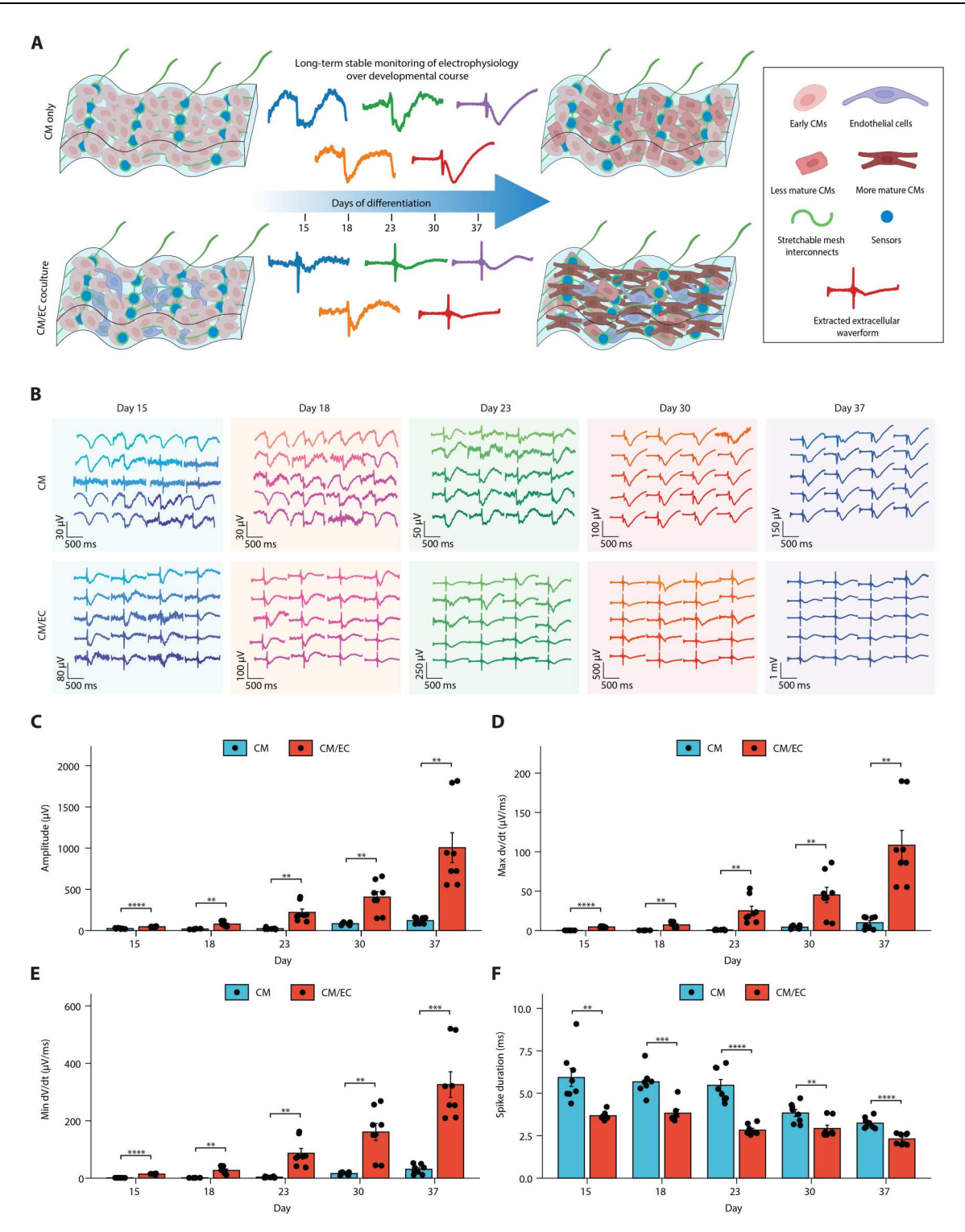
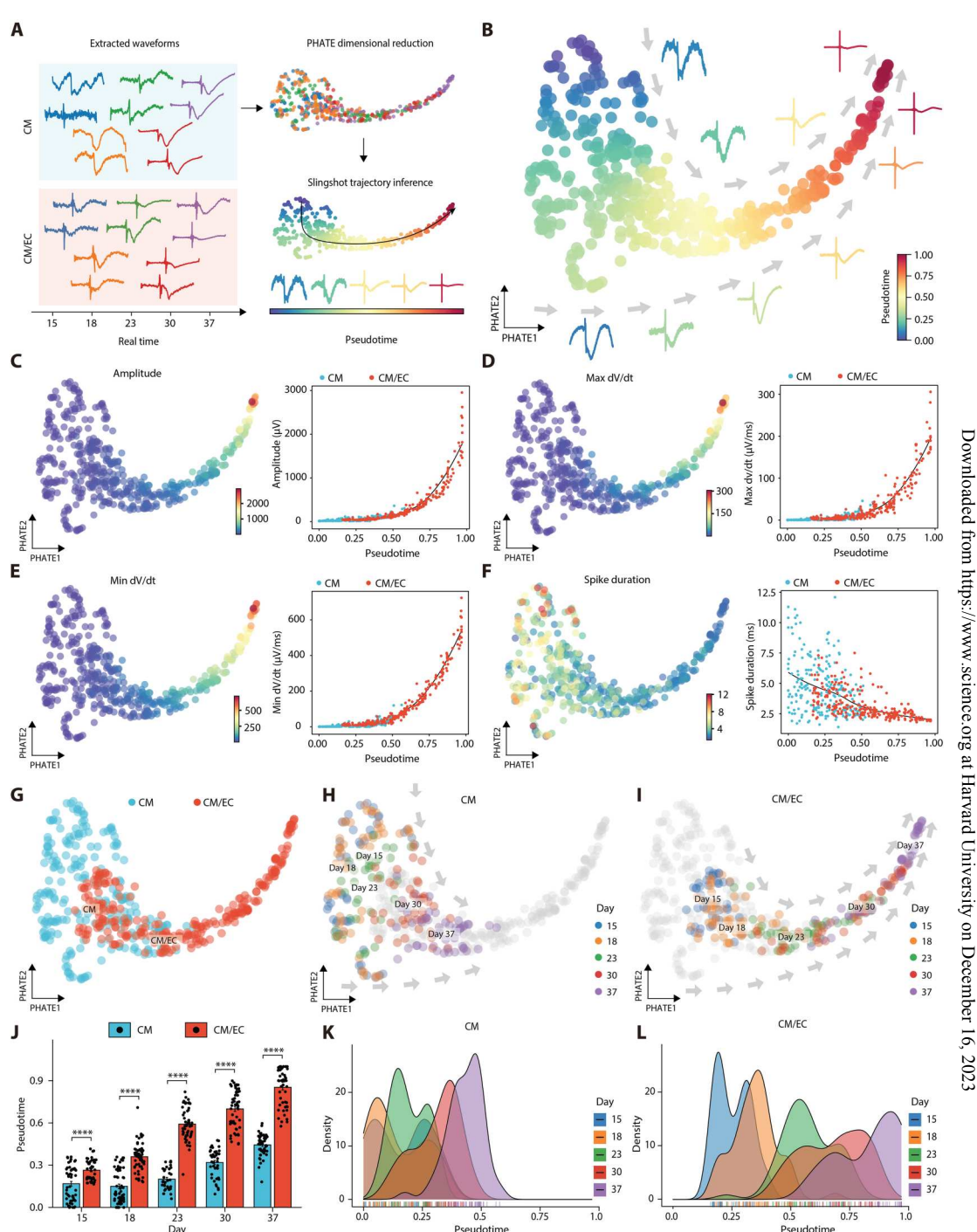


Fig. 3. Long-term stable recording reveals that hiPSC-ECs improved the electrical maturation of hiPSC-CMs over the course of development. (A) Schematics of hiPSC-CMs and hiPSC-CMs/hiPSC-ECs integrating with mesh nanoelectronics for long-term stable, continuous electrical measurement over the course of development. (B) Representative extracted channel-averaged spike waveforms at days 15, 18, 23, 30, and 37 of hiPSC-CM differentiation (days 4, 7, 12, 19, and 26 following reseeding onto stretchable mesh nanoelectronics) for hiPSC-CMs (top) and hiPSC-CMs/hiPSC-ECs (bottom). (C to F) Statistical summary of spike waveform features of hiPSC-CMs and hiPSC-CMs/hiPSC-ECs at days 15, 18, 23, 30, and 37 of differentiation. Data are means \pm SEM; ***P < 0.001 and ****P < 0.0001 by two-tailed, unpaired t test. Each dot represents averaged features from one group of samples, n = 8. Every group has 16 channels, and every four groups of samples are cultured in one well.

Fig. 4. Pseudotime analysis of electrical signals reveals that hiPSC-ECs accelerated the electrical maturation of hiPSC-CMs. (A) Schematics of the pseudotime trajectory inference procedure for the long-term electrical signal analysis. Waveforms ordered by days of differentiation show phenotypic variation within any given time point and across different differentiation conditions (left). Pseudotime orders the waveform across all different time points and differentiation conditions by first using PHATE for dimensional reduction and then using Slingshot for trajectory inference to project the electrical waveform into a continuous pseudotime spectrum (right). (B) PHATE plot showing all the pseudotime-ordered electrical waveform profiles of hiPSC-CMs/hiPSC-ECs and hiPSC-CMs from all channels in four groups of samples recorded at days 15, 18, 23, 30, and 37 of differentiation. Each dot represents a channelaveraged electrical waveform and colors represent the inferred pseudotime from Slingshot. (C to F) Projection of the extracted electrical features into the PHATE manifold. (G) PHATE plot showing all the electrical waveform profiles colorcoded by hiPSC-CMs or hiPSC-CMs/ hiPSC-ECs. (H and I) PHATE plot showing all the electrical waveform profiles of hiPSC-CMs in (H) and hiPSC-CMs/hiPSC-ECs in (I). Each dot represents a channel-averaged electrical waveform and colors represent days of differentiation. (J) Barplot showing the pseudotime value of hiPSC-CMs and hiPSC-CMs/hiPSC-ECs at days 15, 18, 23, 30, and 37 of differentiation. Data are means \pm SEM; ****P < 0.0001 by two-tailed, unpaired t test. Each dot represents a channel-averaged electrical waveform from all channels in four groups of samples. (K and L) Density plot showing the distribution of the pseudotime value of hiPSC-CM (K) and hiPSC-CMs/hiPSC-EC coculture (L) at days 15, 18, 23, 30, and 37 of differentiation.



distributed from the middle to the end. There were some overlaps between two conditions in the middle part of the trajectory (Fig. 4G). Second, within both hiPSC-CM and hiPSC-CM/hiPSC-EC samples, there was a continuous electrical development along the pseudotime trajectory from day 15 to day 37, with a gradual increase of electrical phenotype uniformity and narrowing of the projected manifold. The hiPSC-CM/hiPSC-EC samples also showed

higher uniformity compared to hiPSC-CM samples at earlier time points. In addition, cell electrical phenotypes did not form isolated clusters for any given time point along the trajectory (Fig. 4, H and I). Third, mapping the pseudotime into real time showed a gradual increase of the pseudotime from days 15 to 37 with a significantly higher pseudotime value for hiPSC-CM/hiPSC-EC samples compared to hiPSC-CM samples (Fig. 4J). Last, pseudotime distribution

revealed phenotypic variation at each time point with a spanning pseudotime spectrum and confirmed an accelerated shift toward a more mature electrical state in hiPSC-CM/hiPSC-EC samples compared to hiPSC-CM samples (Fig. 4, K and L).

hiPSC-ECs induce hiPSC-CM maturation genes

To better understand which molecular pathways might be involved in EC-mediated CM electrical maturation, we performed scRNAseq in hiPSC-CMs and hiPSC-CMs cocultured with hiPSC-ECs in a 3:1 CM:EC ratio for 2 weeks starting on day 11 of CM differentiation (through day 24 of differentiation) (Fig. 5A). We first performed data integration between hiPSC-CM and hiPSC-CM/ hiPSC-EC samples with the Harmony algorithm (47), which projects cells into a shared embedding for downstream integrative analysis (Fig. 5A and fig. S7A). We observed similar transcriptional profiles across samples within both hiPSC-CMs and hiPSC-CM/ hiPSC-EC coculture, respectively (fig. S7B). We then performed unsupervised clustering analysis on the integrated dataset, which revealed four major cell types including ECs, fibroblast (FB)-like cells, smooth muscle cells (SMCs), and CMs (Fig. 5B). Cell types were annotated according to previous established marker genes. For example, CMs expressed genes encoding troponin (TNNT2), myosin heavy chain 7 (MYH7), and actin alpha cardiac muscle 1 (ACTC1) (48); ECs expressed genes encoding EC adhesion molecule (ESAM) and platelet EC adhesion molecule 1 (PECAM1) (49); FB-like cells expressed collagen-related genes (COL3A1 and COL1A2) (50); and SMCs were characterized by transgelin (TAGLN) and alpha smooth muscle actin (ACTA2) (fig. S7, D and E) (51, 52). We also observed a group of unidentified cells that could potentially be less mature SMCs with lower TAGLN expression observed in mature SMCs but high expression of other genes related to smooth muscle contraction (MYL6, MYL12A, and MYL12B). The unidentified cells also show little endothelial gene expression (ESAM, PECAM1, and KDR) (fig. S7F). Notably, small populations of non-CMs (FB-like cells, SMCs, ECs, and unidentified cells) were observed in hiPSC-CM samples but comprised less than 10% of the total cell population (Fig. 5C and fig. S7C). ECs made up ~11% of the final cell population in the hiPSC-CM/hiPSC-EC coculture samples, which also had a higher percentage of non-CM/non-ECs so that the total CM population was ~50% of total cells (Fig. 5C and fig. S7C). Next, we compared the overall transcriptional maturation level of CMs between hiPSC-CM and hiPSC-CM/hiPSC-EC samples. We found that hiPSC-CM/hiPSC-EC samples had increased expression levels of ACTC1, TNNI3, SCN5A, GJA1, and HOPX in CM (Fig. 5D), suggesting a higher transcriptional maturation level covering many aspects. Immature CMs primarily express slow skeletal troponin I (TNNI1), which is replaced by cardiac troponin I (TNNI3) in mature CMs (53, 54). The upstroke velocity of mature CM electrophysiology is higher due to higher expression of SCN5A and other sodium channels (54, 55). GJA1 is the major protein of gap junctions, which has a crucial role in the synchronized contraction and electrical conduction of the matured CMs (56, 57). HOPX is a key regulator of CM maturation that is up-regulated in the later stages of CM maturation (50). In addition, further subclustering of the CMs identified five distinct CM subtypes (CM1, CM2, CM3, CM4, and CM5) that show different compositions between hiPSC-CMs and hiPSC-CM/hiPSC-ECs. hiPSC-CMs had a higher proportion of CM4 (Fig. 5E), which showed higher expression levels of genes associated with CM proliferation

(e.g., H19 and RPL23) (Fig. 5F), suggesting a more immature phenotype. In contrast, hiPSC-CMs/hiPSC-ECs had a higher proportion of CM5, which had higher expression levels of genes such as NPPA, SMPX, PRRX1, and HOPX. NPPA and SMPX are chamber-specific genes that are suppressed in pacemaker cells, which may suggest a role in suppressing automaticity (58). PRRX1 (encoding paired-related homeobox 1) down-regulation shortens the action potential duration and increases the risk of atrial fibrillation (59, 60), suggesting a potential role for PRRX1 in electrical maturation of hiPSC-CMs. Gene Ontology (GO) analysis revealed that the expression of genes associated with metabolism and cardiac muscle contraction was increased in CM5 (Fig. 5G). These results collectively suggest that hiPSC-ECs shift the hiPSC-CMs toward CM subpopulations with a higher transcriptional maturation level. Furthermore, we found that EC alters the expression of many extracellular matrix (ECM) genes in CMs by comparing hiPSC-CM/hiPSC-EC and hiPSC-CM (fig. S8). The alteration is different for different ECM genes. For example, several collagen genes (COL1A1, COL1A2, and COL3A1) are down-regulated, while the fibronectin gene (FN1) and several glycoprotein genes (POSTN, SPARC, THBS1, and CNN2) are up-regulated. In addition, several integrin genes are also up-regulated (ITGA1, ITGA5, ITGA7, and ITGB1). These together demonstrated a complex alteration of the ECM in hiPSC-CMs by hiPSC-ECs.

To better understand how hiPSC-ECs might change the electrophysiological phenotype of hiPSC-CMs, we compared the electrophysiological waveforms of hiPSC-CMs and hiPSC-CM/hiPSC-EC cocultures and further derived the average log fold change as a function of the spike time (fig. S9, A and B). We observed that the most differential region was distributed within the fast, sharp upstroke and downstroke window immediately after spike initiation. Evaluating changes in the expression levels of the cardiac ion channels, we observed down-regulation of KCNJ5, KCNQ1, CACNA1G, and KCNJ12 and up-regulation of KCNA5, KCNA4, KCND3, KCNK3, CACNA1C, and SCN5A in hiPSC-CMs/PSC-ECs compared to hiPSC-CMs (fig. S9C). The action potential is initiated by the rapid opening of voltage-gated sodium channels (mainly Nav1.5; encoded by SCN5A) (54, 55), and we observed significant up-regulation of SCN5A that mainly contributed to higher upstroke velocity of more matured CMs phenotype upon hiPSC-EC coculture. The plateau phase of the action potential is longer in more matured CMs, due to the higher expression of the calcium channel Cav1.2 core component CACNA1C (56, 61). In addition, we observed significant up-regulation of potassium channel KCND3 and KCNA4, which contributed to the transient outward current in the more matured CMs (62, 63), resulting in the sharper downstroke in hiPSC-CMs/hiPSC-ECs compared to hiPSC-CMs.

CM/EC coculture enhances multiple ligand-receptor pathways

We next asked whether intercellular communications might be altered upon hiPSC-CM/hiPSC-EC coculture. We used CellChat (64) to infer cell-cell communication via ligand-receptor complexes from scRNA-seq data. The results revealed various changes in cell-cell interactions and ligand-receptor interactions affected by hiPSC-CM/hiPSC-EC coculture (Fig. 6 and fig. S10). Specifically, for both hiPSC-CMs alone and hiPSC-CM/hiPSC-EC coculture, interactions were observed between CMs, FB-like cells, ECs, and SMCs (Fig. 6A). EC-CM interactions represented the largest proportion

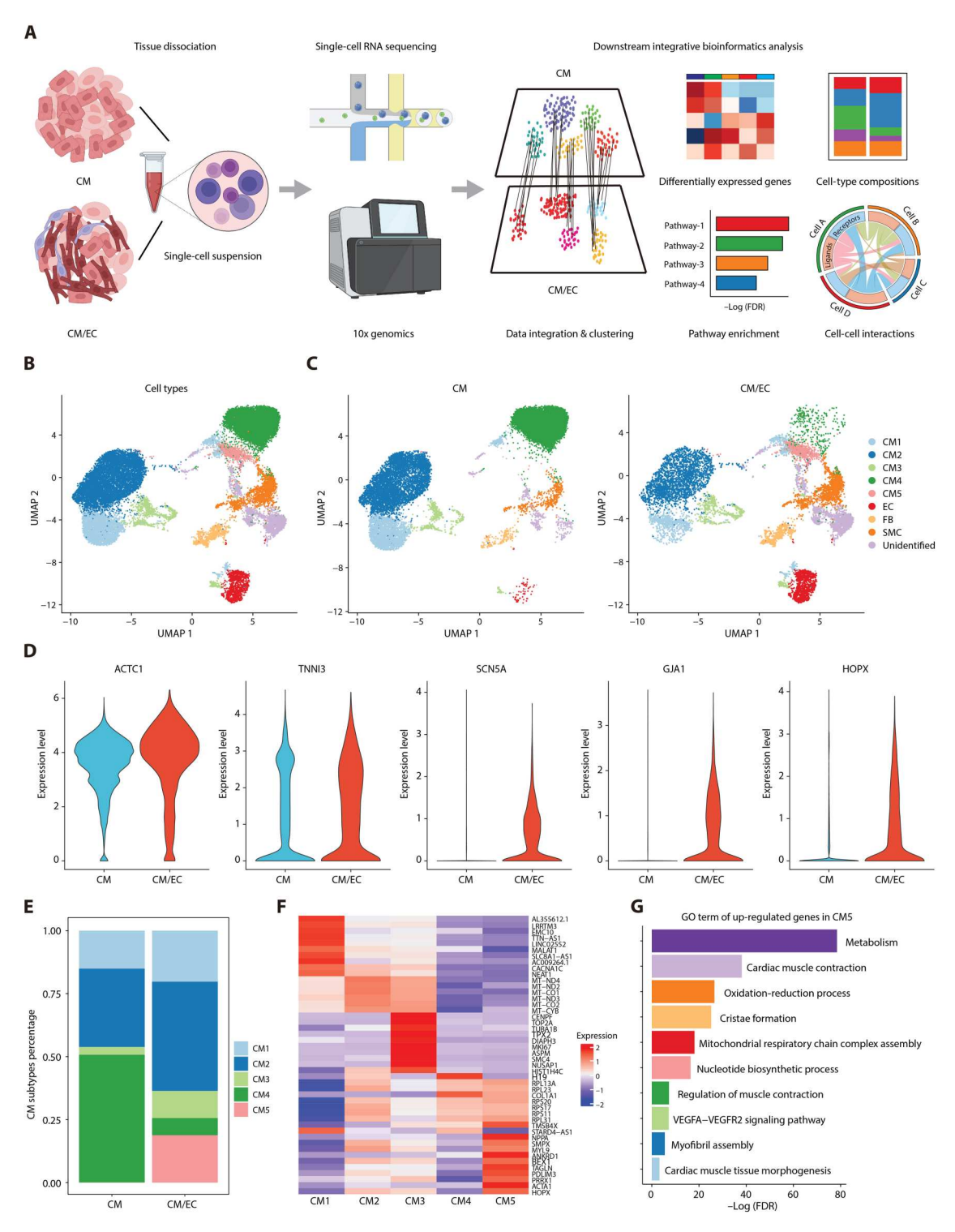


Fig. 5. scRNA-seq reveals that hiPSC-EC coculture up-regulates hiPSC-CM maturation genes. (A) Schematics showing the overview of the scRNA-seq experiment and computational analysis. Created with Biorender.com. (B) Uniform Manifold Approximation and Projection (UMAP) visualization of single-cell RNA expression after integration of data from hiPSC-CM and hiPSC-CM/hiPSC-EC samples. Cells are colored by cell types. (C) UMAP visualization of single-cell RNA expression in hiPSC-CMs (left) and hiPSC-CMs/hiPSC-ECs (right). Cells are colored by cell types. (D) Violin plots showing gene expressions related to CM maturation. Colors correspond to hiPSC-CMs or hiPSC-CMs/hiPSC-ECs. (E) CM subtype percentages in hiPSC-CMs or hiPSC-CMs/hiPSC-ECs. (F) Heatmap showing the up-regulated genes for each CM subtype. (G) Gene Ontology (GO) term analysis for the genes up-regulated in CM5 compared to those in all other CM subpopulations.

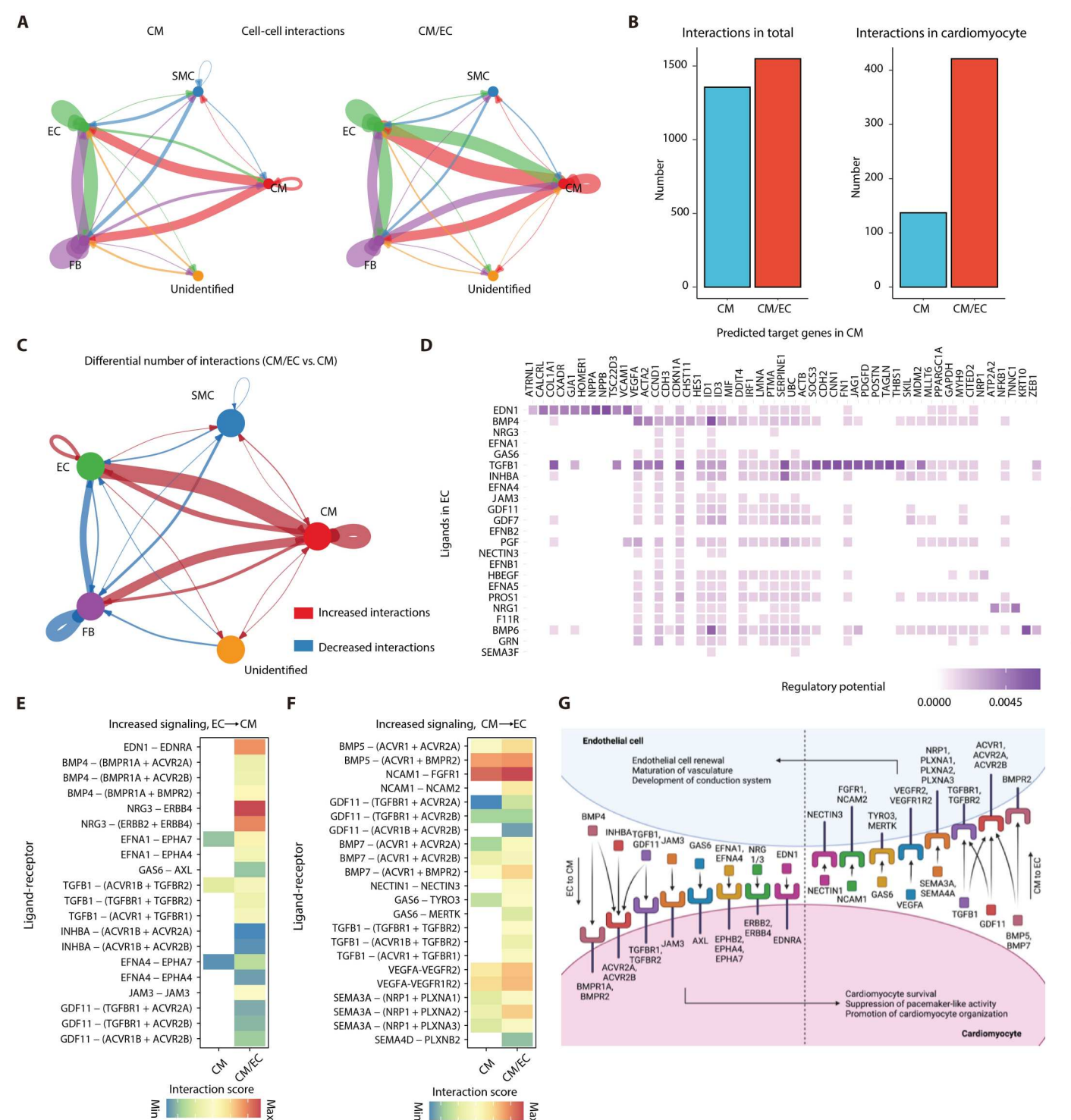


Fig. 6. HiPSC-CM/hiPSC-EC coculture enhances multiple ligand-receptor pathways. (A) Circle plots visualizing ligand-receptor interactions. Interactions between the different cell types were analyzed using CellChat with cells from hiPSC-CMs (left) and hiPSC-CMs/hiPSC-ECs (right). (B) Total ligand-receptor interactions in hiPSC-CMs versus hiPSC-CMs/hiPSC-ECs (left) and ligand-receptor interactions with CMs in hiPSC-CMs versus hiPSC-CMs/hiPSC-ECs (right). (C) Circle plot showing the differential number of interactions comparing hiPSC-CMs/hiPSC-ECs to hiPSC-CMs. (D) Ligand-target matrix showing the regulatory potential between sender (EC) ligand and predicted receiver (CM) target genes analyzed by NicheNet. (E) Heatmap showing the up-regulated ligand-receptor pairs from EC to CM by comparing hiPSC-CMs/hiPSC-ECs to hiPSC-CMs. (F) Heatmap showing the up-regulated ligand-receptor pairs from CM to EC by comparing hiPSC-CMs/hiPSC-ECs to hiPSC-CMs. (G) Schematics showing the proposed intercellular communication model between EC and CM in hiPSC-CM/hiPSC-EC coculture mediated by multiple ligand-receptor interactions. Created with Biorender.com

of the cell-cell interactions in the hiPSC-CM/hiPSC-EC sample. We identified a small population of FB-like cells in our scRNA-seq analysis, due to challenges in achieving 100% purity with current differentiation protocols (65), and consistent with the previous scRNA-seq study of hiPSC-CMs (50). We found that hiPSC-CMs/hiPSC-ECs had a higher number of cell-cell interactions in total compared to hiPSC-CMs and much higher cell-cell interactions in CMs (Fig. 6B). The overall signaling patterns showed that the increase in interactions was predominantly caused by enhanced incoming and outgoing signals in CMs and ECs (fig. S10, A and C). Evaluation of the differential intercellular communications revealed upregulated CMs-ECs, CMs-FBs, and CMs-CMs interactions in hiPSC-CM/hiPSC-EC coculture (Fig. 6C and fig. S10B).

We then focused on the intercellular communications between CMs and ECs. The up-regulated ligand-receptor pairs between CMs and ECs in the hiPSC-CM/hiPSC-EC coculture covered a broad family of signaling pathways such as NRG, endothelin-1, ephrin, transforming growth factor (TGF), bone morphogenetic protein (BMP), and vascular endothelial growth factor (VEGF) (fig. S10D). To further gain insight into the ligand activity and their potential affected genes in the receiver cells, we performed the ligandreceptor target analysis using the NicheNet algorithm (66). We first used ECs as the sender cell type and CMs as the receiver cell type (Fig. 6D). The results revealed multiple enhanced ligand activities in ECs such as EDN1, BMP4, NRG3, EFNA1, TGFB1, and INHBA. Furthermore, the predicted ligand-target regulatory network suggested that the gene expression changes in CMs were mediated by the coordination of multiple ligand activities from ECs. For example, the expression of the gap junction gene GJA1 in CMs could potentially be affected by EDN1, TGFB1, and BMP6 ligand activity from ECs. In addition, individual ligand activity might also regulate multiple target genes. For example, EDN1 might regulate GJA1, NPPA, and NPPB expression, and BMP4 might regulate VEGFA, ID1, and ID3 expression. We then repeated the NicheNet analysis but changed CMs to the sender cell type and ECs to the receiver cell type (fig. S11). The results also demonstrated up-regulated multiple ligand activity in CMs such as VEGFA, SEMA3A, TGFB1, GDF11, NCAM1, and GAS6, which could subsequently target a series of genes in ECs.

Using the predicted ligands from NicheNet analysis, we further revealed the increased interaction between the predicted ligands and the corresponding receptors in the hiPSC-CMs/hiPSC-ECs compared to hiPSC-CMs in both EC-to-CM (Fig. 6E) and CMto-EC interactions (Fig. 6F). EC (ligand)-to-CM (receptor) signaling pathways up-regulated in our scRNA-seq dataset included several members of the TGF superfamily [TGFB1, bone morphogenic protein 4 (BMP4), inhibin A, and growth differentiation factor 11 (GDF11)], NRG3, and ephrins (Fig. 6E). TGFB1 is secreted by multiple cell types, including ECs, and is involved in the CM response to pressure overload via TGFBR1/2 (67). BMP4 is involved in the formation of the pacemaker region in developing hearts via regulation by short stature homeobox 2 (68). TGFB1 and BMP4, as well as inhibin A and GDF11, can all act via activin type II receptor signaling, but with different effects depending on the ligand, to regulate CM renewal (69). Unexpectedly, while our group has previously studied GDF11 in the context of cardiac hypertrophy (70), we are not aware of a known role for GDF11 signaling in early hiPSC-CM maturation—these unbiased results suggest that GDF11 signaling may also play a role in early cardiac development.

NRGs bind to the ErbB2/4 tyrosine kinases to exert a prosurvival effect on CMs (71). NRG3 is primarily thought to regulate the nervous system (72), but the closely related NRG1 may suppress the formation of pacemaker-like PSC-CMs, instead of directing differentiating PSC-CMs toward chamber-specific subtypes (6). Ephrins play a role in normal electrical signaling in the heart, as deletion of EphA4 alters electrocardiographic recordings in rats with absent p waves, QT interval prolongation, and enlarged QRS voltages (73). These findings suggest that there is not a single pathway that contributes to EC-mediated maturation of CMs and that multiple mechanisms act in synchrony to achieve maturation of PSC-CMs.

Similarly, CMs act in cross-talk with ECs to affect EC phenotype, which is consistent with previous findings (12). CM (ligand)—to—EC (receptor) signaling pathways up-regulated in our scRNA-seq dataset included VEGF, semaphorin 3A, and neural cell adhesion molecule 1 (NCAM1) (Fig. 6F). VEGF can have pro-angiogenic effects on ECs but may also serve in an autocrine role to promote CM survival (74, 75). Semaphorin 3A may play an important role in the development of the cardiac conduction system (76). NCAM1 is also important for the development of the ventricular conduction system (77). Thus, there may be a synergistic effect between CMs and ECs in promoting development of the other cell type.

These results suggest that there is not a single mechanism responsible for EC-mediated CM maturation; rather, several pathways are coordinated in the presence of ECs to promote CM maturation (Fig. 6G).

DISCUSSION

CM/EC coculture has previously been shown to be mutually beneficial to both cell types (4-12), and, in this study, we sought to understand how hiPSC-ECs can accelerate electrical maturation of hiPSC-CMs. ECs and CMs participate in cross-talk via paracrine signaling as well as direct cell-to-cell contact (78). Here, the stretchable mesh nanoelectronics approach revealed the extraordinary electrical maturation of hiPSC-CMs by hiPSC-ECs in 3D human cardiac microtissues. Pseudotime analysis of the electrical signals illustrated that hiPSC-CMs exhibited markedly more organized electrical morphology at earlier time points in the presence of hiPSC-ECs. Changes in ion channel gene expression with hiPSC-CM/hiPSC-EC coculture revealed that ECs may predominantly promote the expression of ion channels involved in the rapid depolarization and early repolarization phases of the cardiac action potential. Stage-specific scRNA-seq data revealed that hiPSC-CM/ hiPSC-EC coculture leads to the activation of multiple ligand-receptor pathways, suggesting that CM/EC cross-talk is necessary for proper CM development. These results demonstrate that PSC-ECs may accelerate PSC-CM maturation in vitro via a coordinated process through multiple ligand-receptor pathways.

Specifically, we introduced stretchable mesh nanoelectronics to study electrical and mechanical integration in 3D cardiac microtissues. This technique revealed temporal electrophysiology dynamics in developing 3D cardiac microtissues, demonstrating that hiPSC-ECs accelerated hiPSC-CM electrical maturation. Notably, most methods to study cardiac electrical signaling in vitro require evaluation either as bulk tissues, which have low resolution, or in monolayer culture, which do not adequately recapitulate normal development in 3D as occurs during embryogenesis. This makes

it particularly difficult to study the effects of cell-cell interactions, as when studying the synergistic effects between different cell types is required. In addition, stretchable mesh nanoelectronics also allow for long-term stable, continuous recording of the 3D cardiac microtissue electrical activities at millisecond temporal and cellular resolution, which reveals the notable changes in our system when hiPSC-CMs were cultured alone versus with hiPSC-ECs.

In addition, we applied ML-based pseudotime analysis, previously mainly used for single-cell transcriptomics data analysis, to analyze the long-term stable electrical measurement from the same 3D cardiac microtissues, which reconstructed the electrical phenotypic evolution spectrum by ordering the electrical waveform from multiple discrete time points over the developmental course into a continuous progression path. The application of the pseudotime inference to the electrical waveform fills an important gap for quantifying cardiac electrical phenotype, which would be difficult if using any single extracted electrical features from the high-dimensional waveform data. With the inferred trajectory, we successfully depicted the dynamical change of electrical features and the phenotypic variation for each time point along the trajectory. We found that electrical phenotypes did not form isolated clusters for any given time point in the trajectory but spanned along the path and overlapped between different time points. Furthermore, we found the segregation and the phenotypic overlap of the trajectory for hiPSC-CMs/hiPSC-ECs and hiPSC-CMs. We further confirmed an accelerated shift toward a more mature electrical phenotype in hiPSC-CM/hiPSC-EC cocultures compared to hiPSC-CMs.

Using scRNA-seq, we observed differential expression of cardiac ion channels, which support the differences in phenotype between hiPSC-CM versus hiPSC-EC/hiPSC-CM samples. SCN5A encodes for Nav1.5, which is responsible for depolarization during phase 0 of the action potential via I_{Na}. The rapid repolarization phase (phase 1) involves efflux of potassium ions via Kv4.3 (encoded by KCND3, contributing to Ito), Kv1.4 (encoded by KCNA4, contributing to Ito), and Kur (via Kv1.5 (KCNA5), all of which were up-regulated with EC coculture. In contrast, KCNQ1 (encoding Kv7.1), KCNJ12 (encoding Kir2.2), and KCNJ5 (encoding Kir3.4) are primarily involved in phases 3 and 4 of the cardiac action potential and were down-regulated with hiPSC-EC coculture. These findings suggest that ECs may help fine-tune the balance of potassium channels throughout the cardiac action potential to enable the electrical maturation of hiPSC-CMs. Moreover, we identified multiple ligand-receptor interactions up-regulated with hiPSC-CM/hiPSC-EC coculture, such as NRG, endothelin-1, ephrin, TGF, BMP, and VEGF, revealing a coordinated multifactorial mechanism of ECmediated CM electrical maturation.

In conclusion, this work applied stretchable mesh nanoelectronics to understand how electrophysiological changes occur at multiple points within 3D human cardiac microtissues over time. Use of this technology enabled the discovery of substantial changes in the electrical phenotype of hiPSC-CMs that are accelerated in the presence of hiPSC-ECs. Ion channel expression patterns at a single-cell level correlated with measured electrical signals of hiPSC-CMs, with hiPSC-EC promoting increased expression of ion channels involved in phase 0/1 of the action potential. Notably, our data revealed that multiple communication pathways likely mediate electrical maturation of 3D cardiac microtissues via cross-talk between hiPSC-CMs and hiPSC-ECs. These findings suggest that single gene or single pathway approaches to driving

hiPSC-CM electrical maturation and coordination may be inadequate; rather, systems-wide approaches to understanding integration of intercellular communication will be essential. These systems should also consider the synergistic effects of multiple cell types in addition to CMs and ECs, such as FBs, SMCs, pericytes, and immune cells, which may modulate both CM and EC phenotype. Last, this work demonstrated the integration of tissue-embedded stretchable electronics, ML-based algorithms for high-dimensional electrical recording data analysis, and stage-specific scRNA-seq as a multimodal method for charting of cell functional and transcriptional types and states, which will offer unlimited access to unravel the stem cell functional maturation across different types of cardiac tissues and protocols.

MATERIALS AND METHODS

Cell line maintenance

The human UCSD142i-86-1 iPSC line (abbreviated UCSD iPSCs) was derived from FBs donated by an adult female donor to K. Frazer's laboratory at University of California San Diego (distributed by WiCell). Either StemFlex (Thermo Fisher Scientific) or mTeSR Plus (StemCell Technologies) was used for cell maintenance. Cells were passaged every 3 to 4 days onto Geltrex-coated plates [Geltrex (Thermo Fisher Scientific) used at 1:100 dilution in Dulbecco's modified Eagle's medium/F12]. The ROCK inhibitor Y-27632 2HCl (Selleck Chemicals) included in the maintenance media (5 μ M Y-27632) was used for 24 hours after plating and then changed to fresh maintenance media the next day.

Differentiation of hiPSCs into cardiomyocytes

hiPSCs were seeded into 10-cm tissue culture plates and then allowed to grow for ~4 days until the cells became ~70% confluent. CMs were differentiated from iPSCs as previously described (79) [protocol originally adapted from Lian et al. (35)]. Media were changed to RPMI 1640 + B27 + ascorbic acid (RPMI/B27/AA) containing the GSK3 inhibitor CHIR99021 (Selleck Chemicals) (6 µM) on day 0 of CM differentiation. On day 2 of differentiation, media were changed to RPMI/B27/AA containing the Wnt antagonist IWP-4 (Reprocell) (5 μM). On day 4 of differentiation, media were changed to fresh RPMI/B27/AA, and on day 7 of differentiation, basal media were changed to RPMI/B27 + insulin (10 µg/ml), with media subsequently changed every 2 to 3 days with RPMI/B27/ insulin. Beating of CMs was usually observed between days 7 and 9 of differentiation. CMs were dissociated using the STEMdiff Cardiomyocyte Dissociation Kit (StemCell Technologies) and replated onto Geltrex-coated plates for further assay.

Differentiation of hiPSCs into endothelial cells

We differentiated hiPSCs into ECs according to the protocol previously described by Patsch $\it et~al.~(36)$ and then adapted for differentiation in 3D culture. In brief, hiPSCs were dissociated from 10-cm plates using ReLeSR (StemCell Technologies) according to the manufacturer's instructions. Cells were seeded into 125-ml Erlenmeyer flasks at 200,000 cells/ml in 20 ml of StemScale media (Thermo Fisher Scientific) containing 10 μM Y-27632 and then placed on a plate shaker rotating at 70 rpm. Media were changed to fresh StemScale media the next day to remove the ROCK inhibitor. EC differentiation began 4 days after seeding, when spheroids reached approximately 300 μm in diameter. On day 0 of differentiation,

media were changed to N2B27 medium containing 7 µM CHIR99021 and BMP-4 (25 µg/ml) and incubated for 3 days without media change. On day 3 of differentiation, media were changed to StemPro-34 containing GlutaMAX (Thermo Fisher Scientific) with 2 µM forskolin (Selleck Chemicals) and VEGF (200 ng/ ml) (PeproTech). This same media composition with StemPro-34, forskolin, and VEGF was changed fresh daily for 3 days through day 5 of differentiation. On day 6 of differentiation, spheroids were dissociated using 0.5% trypsin-EDTA diluted 1:3 in phosphate-buffered saline (PBS) for ~5 min. CD144+ ECs were sorted using magnetic microbeads using magnetic-activated cell sorting columns (Miltenyi Biotec) according to the manufacturer's instructions. Sorted CD144+ ECs were replated on Geltrex-coated 10-cm plates and allowed to proliferate for 3 to 7 days in StemPro-34 containing GlutaMAX and VEGF (50 ng/ml) and then redissociated with trypsin-EDTA and replated again onto Geltrex-coated plates for assay.

Coculture of hiPSC-CMs and hiPSC-ECs

hiPSC-CMs on days 10 to 12 of differentiation and PSC-ECs on days 13 to 20 of differentiation were used for replating into 24-well tissue culture plates or mesh nanoelectronics devices precoated with Geltrex and different CM:EC seeding ratios. Total cell number was kept constant (e.g., for mesh nanoelectronics devices, a total of 5 million cells per device were seeded of either CMs alone or at a 3:1 CM:EC ratio; for scRNA-seq analysis, a total of 1 million cells per well of a 24-well plate was seeded with either CMs alone or at a 3:1 CM:EC ratio). Both hiPSC-CMs alone and hiPSC-CMs cocultured with hiPSC-ECs were maintained in StemPro-34 + VEGF (50 ng/ml) after replating for the assay. After 1 to 2 weeks of coculture, cells were dissociated with either trypsin-EDTA or STEMdiff Cardiomyocyte Dissociation Kit for further processing.

Flow cytometry

Cells were dissociated with Trypsin-EDTA (Gibco) or the STEMdiff Cardiomyocyte Dissociation Kit (StemCell Technologies) and $\sim \! 1 \times 10^6$ cells per sample were prepared for flow cytometry to quantify the expression of selected markers of CM maturation. We used the eBioscience Flow Cytometry Staining Buffer Set (Invitrogen) according to the manufacturer's protocols. Extracellular antibody staining was performed first followed by fixation, permeabilization, and staining with intracellular antibodies as previously described (79). We used the Cytek Aurora Spectral Cytometer, BD LSRII, or BD FACSymphony instrument to acquire data and FCS Express 7 software (De Novo Software) to quantify cell percentages and geometric MFIs.

Preparation of stretchable mesh nanoelectronics

Preparations of the stretchable mesh nanoelectronics were based on methods described previously (23, 32, 33, 80). Key steps are described here: 4-inch double-sided polished glass wafers (soda lime glass) were used as the substrate for the stretchable mesh nanoelectronics. The wafers were cleaned by piranha solution (1:3 mixture of 30% hydrogen peroxide and sulfuric acid), followed by rinsing the wafers with deionized (DI) water and by blow-drying with the $\rm N_2$ gas. Then, a sacrificial layer of Ni patterns was prepared by photolithography. Hexamethyldisilazane (HMDS; MicroChem) was spincoated at 4000 rpm for increasing the adhesion of photoresist with the surface of the glass substrate. Then, double-layer photoresists of

LOR 3A (300 nm, MicroChem)/S1805 (500 nm, MicroChem) were spin-coated at 4000 rpm each, followed by baking on a hot plate at 180°C for 5 min and at 115°C for 1 min, respectively. The patterns were exposed with a mask aligner (Karl Suss MA6, 365-nm ultraviolet light) for 40 mJ/cm² and were developed by CD-26 developer (MICROPOSIT) for 70 s to define patterns. Oxygen plasma (Anatech Barrel Plasma System) was used to remove the photoresist residues at 50 W for 30 s. Then, 100-nm Ni was deposited by using a thermal evaporator (Sharon) and followed by a lift-off procedure in remover PG (MicroChem) for 2 hours to define the Ni sacrificial patterns. Next, the SU-8 bottom passivation layer was fabricated by photolithography. SU-8 precursor (SU-8 2000.5, MicroChem) was spin-coated at 4000 rpm, prebaked at 65°/95°C for 2 min each, exposed at a dosage of 200 mJ/cm² by using MA6, postbaked at 65°/95°C for 2 min each, developed (MicroChem) for 60 s by using SU-8 developer, rinsed by isopropyl alcohol for 30 s, blowdried by N₂ gas, and hard-baked at 180°C for 1 hour to define the bottom encapsulation layer of mesh SU-8 patterns. Then, interconnect patterns were defined using HMDS/LOR3A/S1805 bilayer photoresists as described in Ni sacrificial patterns above, followed by using an electron-beam evaporator (Denton) to deposit 5/40/5nm-thick chromium/gold/chromium (Cr/Au/Cr), followed by a standard lift-off procedure to define the interconnects. Next, electrode arrays were defined using HMDS/LOR3A/S1805 bilayer photoresists as described in interconnects above, followed by depositing 5/50-nm-thick chromium/platinum (Cr/Pt) and a standard lift-off procedure to define the electrode arrays. Then, the top encapsulation layer of SU-8 mesh patterns was defined using the method as described in bottom SU-8 above. Next, the flexible flat cable (Molex) was soldered onto the I/O pads using a flip-chip bonder (Finetech Fineplacer), followed by gluing a culture chamber onto the substrate wafer by using a bio-compatible adhesive (Kwik-Sil, WPI). Then, Pt black was electroplated on the electrode arrays using a precursor of chloroplatinic acid (H₂PtCl₆) solution (0.08 weight %, Sigma-Aldrich). The device was then rinsed with DI water and blowdried by N₂ gas. Last, stretchable mesh nanoelectronics were released by using Ni etchant (Transene) for 4 hours to completely release the mesh electronics from the glass substrate. Then, the devices were ready for subsequent sterilization steps before cell culture.

Integration of mesh nanoelectronics with hiPSC-CMs and hiPSC-ECs

The mesh nanoelectronics were released and rinsed with DI water before immersing in 70% ethanol at room temperature to sterilize. Then, the mesh nanoelectronics were sequentially coated with poly-D-lysine hydrobromide (0.1 mg/ml) (Sigma-Aldrich) and Matrigel solution (100 µg/ml) (Corning) before cell seeding. Last, 60 µl of liquid Matrigel (10 mg/ml) solution was added to the cell culture chamber on ice, and then incubated at 37°C for 30 min to cure the Matrigel hydrogel layer. hiPSC-CMs on day 11 of differentiation and hiPSC-ECs on day 14 of differentiation were integrated with mesh nanoelectronics. A total of 5 million cells per mesh nanoelectronics were seeded at a 3:1 CM:EC ratio. Five million hiPSC-CMs alone were also integrated with mesh nanoelectronics as control sample. Both hiPSC-CMs alone and hiPSC-CMs cocultured with hiPSC-ECs were maintained in StemPro-34 + VEGF (50 ng/ml). Five micromolar rock inhibitor (Y27632) was applied in the first 24 hours to improve the cell viability.

Electrophysiological recording

The BlackRock CerePlex Direct voltage amplifier along with a 32-channel BlackRock μ digital headstage was connected to the device for electrical recording. The cell culture medium was grounded by a platinum (Pt) electrode. Another Pt electrode was also used as a reference electrode. The whole setup was placed into a Faraday cage to block the noise. A sampling rate of 30,000 Hz was used for the electrical recording. The cell electrical activities were recorded weekly.

Immunostaining and imaging

The staining was performed as previously reported (81). Briefly, samples were first placed in an X-CLARITY hydrogel polymerization device for 4 hours at 37°C with -90-kPa vacuum and then placed in the X-CLARITY electrophoretic tissue clearing chamber to extract electrophoretic lipids. For the staining, the primary antibodies, TNNT2 and CD31, were incubated at 4°C for 4 days and the secondary antibodies were incubated at 4°C for 2 days. The samples were submerged in optical clearing solution and embedded in 1% agarose gel before imaging using Leica TCS SP8 confocal microscopy.

Analysis of electrical data

We used custom MATLAB (version R2021a) code to extract electrical waveforms and the features. Each raw voltage trace was first smoothed using the "smoothdata()" function, and spike detection was performed with the "findpeaks()" function. The threshold for spike waveform was set by using 3* SD from the mean of the smoothed traces. Then, all the spike waveforms detected from each channel were averaged for feature detections. Amplitude was computed as the voltage difference between the maximum and the minimum value of the averaged spike waveform. Next, the derivative of the average spike waveform was computed. The maximum dV/dt was calculated as the maximum derivative value, while the minimum dV/dt was calculated as the absolute value of the minimum derivative value. The spike duration was calculated as the time difference between maximum dV/dt and minimum dv/dt.

For the electrical pseudotime trajectory inference, we combined all the extracted high-dimensional electrical waveforms from both hiPSC-CM samples and hiPSC-CM/hiPSC-EC samples across all different days of electrical recordings. The electrical waveforms were then used as the features input to PHATE (45) (version 1.0.7) (https://github.com/KrishnaswamyLab/phateR) and were projected into a 2D PHATE-embedding space with the function "phate()" using default parameters. We next extracted the first two PHATE dimension values and used these two dimensions as input for Slingshot (46) (version 2.4.0) (https://github.com/ kstreet13/slingshot) to perform the pseudotime trajectory inference with the function "slingshot()" using the default parameters. The trajectory curve was constructed from the Slingshot output, and each projected waveform data point was assigned a pseudotime value according to its projected position in the trajectory curve. Using this combined computational approach, we projected longterm electrical recording data from hiPSC-CMs and hiPSC-CM/ hiPSC-EC samples to a joint pseudotime trajectory that map the electrical phenotypic transition throughout cardiac development.

Quantification of sarcomere alignment

We used a Sarcomere Organization Texture Analysis algorithm that uses Haralick texture structures to quantify sarcomere alignment as previously described (*37*).

Preparation of cells for scRNA-seq

After 14 days of coculture, cells were dissociated from 24-well plates using the STEMdiff Cardiomyocyte Differentiation Kit and then strained through a 70-µm filter to remove clumps. Cells were resuspended at 1000 cells/µl in PBS containing 0.04% bovine serum albumin. Samples were prepared with the 10X Genomics Chromium Single Cell 3' v3 Reagent Kit according to the 10X Genomics Single Cell Protocols Cell Preparation Guide and then sequenced using the Illumina NovaSeq. The reference genome used was the *Homo sapiens* (human) genome assembly GRCH38 (hg38). Raw and processed data files were deposited to Gene Expression Omnibus at accession number GSE210513.

Single-cell RNA sequencing data analysis

The Cell Ranger 6.1.1 pipeline (10X Genomics) was first used to perform read alignments to the reference human genome GRCh38. Default parameters were used to align reads and to count unique molecular identifier to generate gene-by-cell expression matrices. The R package Seurat (82) (version 4.0.6) (https:// satijalab.org/seurat/index.html) was then used to perform downstream analysis for the gene-by-cell expression matrices. Cells were filtered to retain only higher-quality cells (mitochondrial reads <25%, genes detected >200 and < 9000). The expression matrices were normalized and scaled with "NormalizeData()," "Find-VariableFeatures()," and "ScaleData()" using the default parameters. Then, we use "RunPCA()" to perform dimensional reduction. The hiPSC-CM and hiPSC-CM/hiPSC-EC samples were then integrated with the Harmony (47) algorithm by using the "RunHarmony()" function. The integrated data were next visualized with Uniform Manifold Approximation and Projection (UMAP) with "RunUMAP()" using the first 30 dimensions from the Harmony output. Unsupervised clustering was performed with "FindNeighbors()" and "FindClusters()" using the first 30 dimensions from the Harmony output and 0.2 resolution. The marker genes were then compared with previous publications for cell-type annotation. Differentially expressed genes were generated with Seurat's Wilcoxon rank sum test, and the GO analysis for the differentially expressed genes was performed with Cytoscape's (83) functional enrich-

The R package CellChat (64) (version 1.4.0) was used for cell-cell interaction analysis. We followed the standard tutorial "Comparison analysis of multiple datasets using CellChat" from the CellChat GitHub repository (https://github.com/sqjin/CellChat) to compare the interaction patterns between hiPSC-CM and hiPSC-CM/hiPSC-EC samples. We then further followed the tutorial from the R package NicheNet (66) (https://github.com/saeyslab/nichenetr) to identify the ligand-target matrix by using EC as sender cell types and CM as receiver cell types and vice versa.

Statistical analysis

Statistical analysis was performed with the R package ggpubr (https://rpkgs.datanovia.com/ggpubr). The sample sizes for replicates and detailed statistics used are presented in the figure legends.

Supplementary Materials

This PDF file includes:

Figs. S1 to S11 Table S1

REFERENCES AND NOTES

- R. Romagnuolo, H. Masoudpour, A. Porta-Sanchez, B. Qiang, J. Barry, A. Laskary, X. Qi, S. Masse, K. Magtibay, H. Kawajiri, J. Wu, T. Valdman Sadikov, J. Rothberg, K. M. Panchalingam, E. Titus, R. K. Li, P. W. Zandstra, G. A. Wright, K. Nanthakumar, N. R. Ghugre, G. Keller, M. A. Laflamme, Human embryonic stem cell-derived cardiomyocytes regenerate the infarcted pig heart but induce ventricular tachyarrhythmias. Stem Cell Reports 12, 967–981 (2019).
- Y. W. Liu, B. Chen, X. Yang, J. A. Fugate, F. A. Kalucki, A. Futakuchi-Tsuchida, L. Couture, K. W. Vogel, C. A. Astley, A. Baldessari, J. Ogle, C. W. Don, Z. L. Steinberg, S. P. Seslar, S. A. Tuck, H. Tsuchida, A. V. Naumova, S. K. Dupras, M. S. Lyu, J. Lee, D. W. Hailey, H. Reinecke, L. Pabon, B. H. Fryer, W. R. MacLellan, R. S. Thies, C. E. Murry, Human embryonic stem cell-derived cardiomyocytes restore function in infarcted hearts of non-human primates. Nat. Biotechnol. 36. 597–605 (2018).
- J. J. Chong, X. Yang, C. W. Don, E. Minami, Y. W. Liu, J. J. Weyers, W. M. Mahoney, B. Van Biber,
 S. M. Cook, N. J. Palpant, J. A. Gantz, J. A. Fugate, V. Muskheli, G. M. Gough, K. W. Vogel,
 C. A. Astley, C. E. Hotchkiss, A. Baldessari, L. Pabon, H. Reinecke, E. A. Gill, V. Nelson,
 H. P. Kiem, M. A. Laflamme, C. E. Murry, Human embryonic-stem-cell-derived cardiomyocytes regenerate non-human primate hearts. *Nature* 510, 273–277 (2014).
- X. Qu, C. Harmelink, H. S. Baldwin, Endocardial-myocardial interactions during early cardiac differentiation and trabeculation. Front. Cardiovasc. Med. 9, 857581 (2022).
- P. C. Hsieh, M. E. Davis, L. K. Lisowski, R. T. Lee, Endothelial-cardiomyocyte interactions in cardiac development and repair. *Annu. Rev. Physiol.* 68, 51–66 (2006).
- W. Z. Zhu, Y. Xie, K. W. Moyes, J. D. Gold, B. Askari, M. A. Laflamme, Neuregulin/ErbB signaling regulates cardiac subtype specification in differentiating human embryonic stem cells. Circ. Res. 107, 776–786 (2010).
- K. F. Lee, H. Simon, H. Chen, B. Bates, M. C. Hung, C. Hauser, Requirement for neuregulin receptor erbB2 in neural and cardiac development. *Nature* 378, 394–398 (1995).
- M. Bjarnegard, M. Enge, J. Norlin, S. Gustafsdottir, S. Fredriksson, A. Abramsson, M. Takemoto, E. Gustafsson, R. Fassler, C. Betsholtz, Endothelium-specific ablation of PDGFB leads to pericyte loss and glomerular, cardiac and placental abnormalities. *Development* 131, 1847–1857 (2004).
- D. A. Narmoneva, R. Vukmirovic, M. E. Davis, R. D. Kamm, R. T. Lee, Endothelial cells promote cardiac myocyte survival and spatial reorganization: Implications for cardiac regeneration. *Circulation* 110, 962–968 (2004).
- K. K. Dunn, I. M. Reichardt, A. D. Simmons, G. Jin, M. E. Floy, K. M. Hoon, S. P. Palecek, Coculture of endothelial cells with human pluripotent stem cell-derived cardiac progenitors reveals a differentiation stage-specific enhancement of cardiomyocyte maturation. *Biotechnol. J.* 14, e1800725 (2019).
- P. W. Burridge, S. A. Metzler, K. H. Nakayama, O. J. Abilez, C. S. Simmons, M. A. Bruce, Y. Matsuura, P. Kim, J. C. Wu, M. Butte, N. F. Huang, P. C. Yang, Multi-cellular interactions sustain long-term contractility of human pluripotent stem cell-derived cardiomyocytes. *Am. J. Transl. Res.* 6, 724–735 (2014).
- E. Helle, M. Ampuja, A. Dainis, L. Antola, E. Temmes, E. Tolvanen, E. Mervaala, R. Kivela, HiPS-endothelial cells acquire cardiac endothelial phenotype in co-culture with hiPS-cardiomyocytes. Front. Cell Dev. Biol. 9, 715093 (2021).
- X. Sun, J. Wu, B. Qiang, R. Romagnuolo, M. Gagliardi, G. Keller, M. A. Laflamme, R. K. Li, S. S. Nunes, Transplanted microvessels improve pluripotent stem cell-derived cardiomyocyte engraftment and cardiac function after infarction in rats. Sci. Transl. Med. 12, eaax2992 (2020).
- X. Hong, N. Oh, K. Wang, J. Neumeyer, C. N. Lee, R. Z. Lin, B. Piekarski, S. Emani, A. K. Greene, I. Friehs, P. J. Del Nido, J. M. Melero-Martin, Human endothelial colony-forming cells provide trophic support for pluripotent stem cell-derived cardiomyocytes via distinctively high expression of neuregulin-1. *Angiogenesis* 24, 327–344 (2021).
- D. J. Richards, Y. Li, C. M. Kerr, J. Yao, G. C. Beeson, R. C. Coyle, X. Chen, J. Jia, B. Damon, R. Wilson, E. Starr Hazard, G. Hardiman, D. R. Menick, C. C. Beeson, H. Yao, T. Ye, Y. Mei, Human cardiac organoids for the modelling of myocardial infarction and drug cardiotoxicity. *Nat. Biomed. Eng.* 4, 446–462 (2020).
- Y. Yamamoto, S. Hirose, Y. Wuriyanghai, D. Yoshinaga, T. Makiyama, Electrophysiological analysis of hiPSC-derived cardiomyocytes using a patch-clamp technique. *Methods Mol. Biol.* 2320, 121–133 (2021).
- H. Kim, R. D. Kamm, G. Vunjak-Novakovic, J. C. Wu, Progress in multicellular human cardiac organoids for clinical applications. Cell Stem Cell 29, 503–514 (2022).

- P. Garg, V. Garg, R. Shrestha, M. C. Sanguinetti, T. J. Kamp, J. C. Wu, Human induced pluripotent stem cell-derived cardiomyocytes as models for cardiac channelopathies: A primer for non-electrophysiologists. *Circ. Res.* 123, 224–243 (2018).
- L. Drakhlis, S. Biswanath, C. M. Farr, V. Lupanow, J. Teske, K. Ritzenhoff, A. Franke, F. Manstein, E. Bolesani, H. Kempf, S. Liebscher, K. Schenke-Layland, J. Hegermann, L. Nolte, H. Meyer, J. de la Roche, S. Thiemann, C. Wahl-Schott, U. Martin, R. Zweigerdt, Human heart-forming organoids recapitulate early heart and foregut development. *Nat. Biotech*nol. 39, 737–746 (2021).
- Y. R. Lewis-Israeli, A. H. Wasserman, M. A. Gabalski, B. D. Volmert, Y. Ming, K. A. Ball, W. Yang, J. Zou, G. Ni, N. Pajares, X. Chatzistavrou, W. Li, C. Zhou, A. Aguirre, Self-assembling human heart organoids for the modeling of cardiac development and congenital heart disease. *Nat. Commun.* 12, 5142 (2021).
- R. Feiner, L. Engel, S. Fleischer, M. Malki, I. Gal, A. Shapira, Y. Shacham-Diamand, T. Dvir, Engineered hybrid cardiac patches with multifunctional electronics for online monitoring and regulation of tissue function. *Nat. Mater.* 15, 679–685 (2016).
- B. Tian, J. Liu, T. Dvir, L. Jin, J. H. Tsui, Q. Qing, Z. Suo, R. Langer, D. S. Kohane, C. M. Lieber, Macroporous nanowire nanoelectronic scaffolds for synthetic tissues. *Nat. Mater.* 11, 986–994 (2012).
- J. Liu, T.-M. Fu, Z. Cheng, G. Hong, T. Zhou, L. Jin, M. Duvvuri, Z. Jiang, P. Kruskal, C. Xie, Z. Suo, Y. Fang, C. M. Lieber, Syringe-injectable electronics. *Nat. Nanotechnol.* 10, 629–636 (2015).
- D.-H. Kim, R. Ghaffari, N. Lu, J. A. Rogers, Flexible and stretchable electronics for biointegrated devices. *Annu. Rev. Biomed. Eng.* 14, 113–128 (2012).
- D.-H. Kim, N. Lu, Y. Huang, J. A. Rogers, Materials for stretchable electronics in bioinspired and biointegrated devices. MRS Bull. 37, 226–235 (2012).
- Y. Fang, X. Yang, Y. Lin, J. Shi, A. Prominski, C. Clayton, E. Ostroff, B. Tian, Dissecting biological and synthetic soft-hard interfaces for tissue-like systems. *Chem. Rev.* 122, 5233–5276 (2022).
- A. Prominski, B. Tian, Bridging the gap—Biomimetic design of bioelectronic interfaces. Curr. Opin. Biotechnol. 72, 69–75 (2021).
- J. Li, Y. Liu, L. Yuan, B. Zhang, E. S. Bishop, K. Wang, J. Tang, Y. Q. Zheng, W. Xu, S. Niu, L. Beker, T. L. Li, G. Chen, M. Diyaolu, A. L. Thomas, V. Mottini, J. B. Tok, J. C. Y. Dunn, B. Cui, S. P. Pasca, Y. Cui, A. Habtezion, X. Chen, Z. Bao, A tissue-like neurotransmitter sensor for the brain and gut. *Nature* 606, 94–101 (2022).
- J. Liu, X. Zhang, Y. Liu, M. Rodrigo, P. D. Loftus, J. Aparicio-Valenzuela, J. Zheng, T. Pong, K. J. Cyr, M. Babakhanian, J. Hasi, J. Li, Y. Jiang, C. J. Kenney, P. J. Wang, A. M. Lee, Z. Bao, Intrinsically stretchable electrode array enabled in vivo electrophysiological mapping of atrial fibrillation at cellular resolution. *Proc. Natl. Acad. Sci. U.S.A.* 117, 14769–14778 (2020).
- S.-H. Sunwoo, S. I. Han, H. Kang, Y. S. Cho, D. Jung, C. Lim, C. Lim, M.-j. Cha, S.-P. Lee, T. Hyeon, D.-H. Kim, Stretchable low-impedance nanocomposite comprised of Ag-Au coreshell nanowires and Pt black for epicardial recording and stimulation. *Adv. Mater. Technol.* 5, 1900768 (2020)
- A. Kalmykov, C. Huang, J. Bliley, D. Shiwarski, J. Tashman, A. Abdullah, S. K. Rastogi,
 S. Shukla, E. Mataev, A. W. Feinberg, K. J. Hsia, T. Cohen-Karni, Organ-on-e-chip: Three-dimensional self-rolled biosensor array for electrical interrogations of human electrogenic spheroids. Sci. Adv. 5, eaax0729 (2019).
- P. Le Floch, Q. Li, Z. Lin, S. Zhao, R. Liu, K. Tasnim, H. Jiang, J. Liu, Stretchable mesh nanoelectronics for 3D single-cell chronic electrophysiology from developing brain organoids. *Adv. Mater.* 34, e2106829 (2022).
- Q. Li, K. Nan, P. Le Floch, Z. Lin, H. Sheng, T. S. Blum, J. Liu, Cyborg organoids: Implantation of nanoelectronics via organogenesis for tissue-wide electrophysiology. *Nano Lett.* 19, 5781–5789 (2019).
- X. Wang, R. Feiner, H. Luan, Q. Zhang, S. Zhao, Y. Zhang, M. Han, Y. Li, R. Sun, H. Wang, T.-L. Liu, X. Guo, H. Oved, N. Noor, A. Shapira, Y. Zhang, Y. Huang, T. Dvir, J. A. Rogers, Threedimensional electronic scaffolds for monitoring and regulation of multifunctional hybrid tissues. Extreme Mech. Lett. 35, 100634 (2020).
- X. Lian, J. Zhang, S. M. Azarin, K. Zhu, L. B. Hazeltine, X. Bao, C. Hsiao, T. J. Kamp, S. P. Palecek, Directed cardiomyocyte differentiation from human pluripotent stem cells by modulating Wnt/β-catenin signaling under fully defined conditions. *Nat. Protoc.* 8, 162–175 (2013).
- C. Patsch, L. Challet-Meylan, E. C. Thoma, E. Urich, T. Heckel, J. F. O'Sullivan, S. J. Grainger, F. G. Kapp, L. Sun, K. Christensen, Y. Xia, M. H. Florido, W. He, W. Pan, M. Prummer, C. R. Warren, R. Jakob-Roetne, U. Certa, R. Jagasia, P. O. Freskgard, I. Adatto, D. Kling, P. Huang, L. I. Zon, E. L. Chaikof, R. E. Gerszten, M. Graf, R. Iacone, C. A. Cowan, Generation of vascular endothelial and smooth muscle cells from human pluripotent stem cells. Nat. Cell Biol. 17, 994–1003 (2015).
- M. D. Sutcliffe, P. M. Tan, A. Fernandez-Perez, Y.-J. Nam, N. V. Munshi, J. J. Saucerman, High
 content analysis identifies unique morphological features of reprogrammed cardiomyocytes. Sci. Rep. 8, 1258 (2018).

SCIENCE ADVANCES | RESEARCH ARTICLE

- X. Dai, W. Zhou, T. Gao, J. Liu, C. M. Lieber, Three-dimensional mapping and regulation of action potential propagation in nanoelectronics-innervated tissues. *Nat. Nanotechnol.* 11, 776–782 (2016).
- S. Lee, D. Sasaki, D. Kim, M. Mori, T. Yokota, H. Lee, S. Park, K. Fukuda, M. Sekino, K. Matsuura, T. Shimizu, T. Someya, Ultrasoft electronics to monitor dynamically pulsing cardiomyocytes. *Nat. Nanotechnol.* 14. 156–160 (2019).
- T. Ohya, H. Ohtomo, T. Kikuchi, D. Sasaki, Y. Kawamura, K. Matsuura, T. Shimizu, K. Fukuda, T. Someya, S. Umezu, Simultaneous measurement of contractile force and field potential of dynamically beating human iPS cell-derived cardiac cell sheet-tissue with flexible electronics. *Lab Chip* 21, 3899–3909 (2021).
- 41. H. Gao, F. Yang, K. Sattari, X. Du, T. Fu, S. Fu, X. Liu, J. Lin, Y. Sun, J. Yao, Bioinspired two-inone nanotransistor sensor for the simultaneous measurements of electrical and mechanical cellular responses. *Sci. Adv.* **8**, eabn2485 (2022).
- N. Kumar, J. A. Dougherty, H. R. Manring, I. Elmadbouh, M. Mergaye, A. Czirok, D. Greta Isai, A. E. Belevych, L. Yu, P. M. L. Janssen, P. Fadda, S. Gyorke, M. A. Ackermann, M. G. Angelos, M. Khan, Assessment of temporal functional changes and miRNA profiling of human iPSCderived cardiomyocytes. Sci. Rep. 9, 13188 (2019).
- H. Zhu, K. S. Scharnhorst, A. Z. Stieg, J. K. Gimzewski, I. Minami, N. Nakatsuji, H. Nakano, A. Nakano, Two dimensional electrophysiological characterization of human pluripotent stem cell-derived cardiomyocyte system. Sci. Rep. 7, 43210 (2017).
- 44. W. Saelens, R. Cannoodt, H. Todorov, Y. Saeys, A comparison of single-cell trajectory inference methods. *Nat. Biotechnol.* **37**, 547–554 (2019).
- K. R. Moon, D. van Dijk, Z. Wang, S. Gigante, D. B. Burkhardt, W. S. Chen, K. Yim, A. V. D. Elzen, M. J. Hirn, R. R. Coifman, N. B. Ivanova, G. Wolf, S. Krishnaswamy, Visualizing structure and transitions in high-dimensional biological data. *Nat. Biotechnol.* 37, 1482–1492 (2019).
- K. Street, D. Risso, R. B. Fletcher, D. Das, J. Ngai, N. Yosef, E. Purdom, S. Dudoit, Slingshot: Cell lineage and pseudotime inference for single-cell transcriptomics. *BMC Genomics* 19, 477 (2018).
- I. Korsunsky, N. Millard, J. Fan, K. Slowikowski, F. Zhang, K. Wei, Y. Baglaenko, M. Brenner, P. R. Loh, S. Raychaudhuri, Fast, sensitive and accurate integration of single-cell data with Harmony. *Nat. Methods* 16, 1289–1296 (2019).
- J. M. Churko, P. Garg, B. Treutlein, M. Venkatasubramanian, H. Wu, J. Lee, Q. N. Wessells, S. Y. Chen, W. Y. Chen, K. Chetal, G. Mantalas, N. Neff, E. Jabart, A. Sharma, G. P. Nolan, N. Salomonis, J. C. Wu, Defining human cardiac transcription factor hierarchies using integrated single-cell heterogeneity analysis. *Nat. Commun.* 9, 4906 (2018).
- A. Lother, S. Bergemann, L. Deng, M. Moser, C. Bode, L. Hein, Cardiac endothelial cell transcriptome. Arterioscler. Thromb. Vasc. Biol. 38, 566–574 (2018).
- C. E. Friedman, Q. Nguyen, S. W. Lukowski, A. Helfer, H. S. Chiu, J. Miklas, S. Levy, S. Suo, J. J. Han, P. Osteil, G. Peng, N. Jing, G. J. Baillie, A. Senabouth, A. N. Christ, T. J. Bruxner, C. E. Murry, E. S. Wong, J. Ding, Y. Wang, J. Hudson, H. Ruohola-Baker, Z. Bar-Joseph, P. P. L. Tam, J. E. Powell, N. J. Palpant, Single-cell transcriptomic analysis of cardiac differentiation from human PSCs reveals HOPX-dependent cardiomyocyte maturation. *Cell Stem Cell* 23, 586–598 e588 (2018).
- D. Iyer, L. Gambardella, W. G. Bernard, F. Serrano, V. L. Mascetti, R. A. Pedersen, A. Talasila,
 S. Sinha, Robust derivation of epicardium and its differentiated smooth muscle cell progeny from human pluripotent stem cells. *Development* 142, 1528–1541 (2015).
- H. Zhang, L. Tian, M. Shen, C. Tu, H. Wu, M. Gu, D. T. Paik, J. C. Wu, Generation of quiescent cardiac fibroblasts from human induced pluripotent stem cells for in vitro modeling of cardiac fibrosis. Circ. Res. 125, 552–566 (2019).
- F. B. Bedada, S. S. Chan, S. K. Metzger, L. Zhang, J. Zhang, D. J. Garry, T. J. Kamp, M. Kyba, J. M. Metzger, Acquisition of a quantitative, stoichiometrically conserved ratiometric marker of maturation status in stem cell-derived cardiac myocytes. Stem Cell Rep. 3, 594–605 (2014).
- Y. Guo, W. T. Pu, Cardiomyocyte maturation: New phase in development. Circ. Res. 126, 1086–1106 (2020).
- V. Haufe, J. A. Camacho, R. Dumaine, B. Gunther, C. Bollensdorff, G. S. von Banchet, K. Benndorf, T. Zimmer, Expression pattern of neuronal and skeletal muscle voltage-gated Na⁺ channels in the developing mouse heart. J. Physiol. 564, 683–696 (2005).
- E. Karbassi, A. Fenix, S. Marchiano, N. Muraoka, K. Nakamura, X. Yang, C. E. Murry, Cardiomyocyte maturation: Advances in knowledge and implications for regenerative medicine. Nat. Rev. Cardiol. 17, 341–359 (2020).
- 57. C. W. Lo, Role of gap junctions in cardiac conduction and development. *Circ. Res.* **87**, 346–348 (2000).
- W. M. Hoogaars, A. Engel, J. F. Brons, A. O. Verkerk, F. J. de Lange, L. Y. Wong, M. L. Bakker, D. E. Clout, V. Wakker, P. Barnett, J. H. Ravesloot, A. F. Moorman, E. E. Verheijck, V. M. Christoffels, TBX3 controls the sinoatrial node gene program and imposes pacemaker function on the atria. *Genes Dev.* 21, 1098–1112 (2007).

- F. M. Bosada, M. R. Rivaud, J. S. Uhm, S. Verheule, K. van Duijvenboden, A. O. Verkerk, V. M. Christoffels, B. J. Boukens, A variant noncoding region regulates PRRX1 and predisposes to atrial arrhythmias. *Circ. Res.* 129, 420–434 (2021).
- N. R. Tucker, E. V. Dolmatova, H. Lin, R. R. Cooper, J. Ye, W. J. Hucker, H. S. Jameson, V. A. Parsons, L. C. Weng, R. W. Mills, M. F. Sinner, M. Imakaev, J. Leyton-Mange, G. Vlahakes, E. J. Benjamin, K. L. Lunetta, S. A. Lubitz, L. Mirny, D. J. Milan, P. T. Ellinor, Diminished *PRRX1* expression is associated with increased risk of atrial fibrillation and shortening of the cardiac action potential. *Circ. Cardiovasc. Genet.* 10, e001902 (2017).
- Y. Qu, M. Boutjdir, Gene expression of SERCA2a and L- and T-type Ca channels during human heart development. *Pediatr. Res.* 50, 569–574 (2001).
- 62. E. Giacomelli, V. Meraviglia, G. Campostrini, A. Cochrane, X. Cao, R. W. J. van Helden, A. K. Garcia, M. Mircea, S. Kostidis, R. P. Davis, B. J. van Meer, C. R. Jost, A. J. Koster, H. Mei, D. G. Miguez, A. A. Mulder, M. Ledesma-Terron, G. Pompilio, L. Sala, D. C. F. Salvatori, R. C. Slieker, E. Sommariva, A. A. F. de Vries, M. Giera, S. Semrau, L. G. J. Tertoolen, V. V. Orlova, M. Bellin, C. L. Mummery, Human-iPSC-derived cardiac stromal cells enhance maturation in 3D cardiac microtissues and reveal non-cardiomyocyte contributions to heart disease. Cell Stem Cell 26, 862–879 e811 (2020).
- 63. A. O. Grant, Cardiac ion channels. Circ. Arrhythm. Electrophysiol. 2, 185-194 (2009).
- S. Jin, C. F. Guerrero-Juarez, L. Zhang, I. Chang, R. Ramos, C.-H. Kuan, P. Myung, M. V. Plikus,
 Q. Nie, Inference and analysis of cell-cell communication using CellChat. *Nat. Commun.* 12, 1088 (2021).
- K. Kim, A. Doi, B. Wen, K. Ng, R. Zhao, P. Cahan, J. Kim, M. J. Aryee, H. Ji, L. I. Ehrlich,
 A. Yabuuchi, A. Takeuchi, K. C. Cunniff, H. Hongguang, S. McKinney-Freeman, O. Naveiras,
 T. J. Yoon, R. A. Irizarry, N. Jung, J. Seita, J. Hanna, P. Murakami, R. Jaenisch, R. Weissleder,
 S. H. Orkin, I. L. Weissman, A. P. Feinberg, G. Q. Daley, Epigenetic memory in induced pluripotent stem cells. *Nature* 467, 285–290 (2010).
- R. Browaeys, W. Saelens, Y. Saeys, NicheNet: Modeling intercellular communication by linking ligands to target genes. Nat. Methods 17, 159–162 (2020).
- N. Koitabashi, T. Danner, A. L. Zaiman, Y. M. Pinto, J. Rowell, J. Mankowski, D. Zhang, T. Nakamura, E. Takimoto, D. A. Kass, Pivotal role of cardiomyocyte TGF-β signaling in the murine pathological response to sustained pressure overload. *J. Clin. Invest.* 121, 2301–2312 (2011).
- S. Puskaric, S. Schmitteckert, A. D. Mori, A. Glaser, K. U. Schneider, B. G. Bruneau, R. J. Blaschke, H. Steinbeisser, G. Rappold, Shox2 mediates Tbx5 activity by regulating Bmp4 in the pacemaker region of the developing heart. *Hum. Mol. Genet.* 19, 4625–4633 (2010).
- D. Dogra, S. Ahuja, H. T. Kim, S. J. Rasouli, D. Y. R. Stainier, S. Reischauer, Opposite effects of Activin type 2 receptor ligands on cardiomyocyte proliferation during development and repair. *Nat. Commun.* 8, 1902 (2017).
- F. S. Loffredo, M. L. Steinhauser, S. M. Jay, J. Gannon, J. R. Pancoast, P. Yalamanchi, M. Sinha, C. Dall'Osso, D. Khong, J. L. Shadrach, C. M. Miller, B. S. Singer, A. Stewart, N. Psychogios, R. E. Gerszten, A. J. Hartigan, M. J. Kim, T. Serwold, A. J. Wagers, R. T. Lee, Growth differentiation factor 11 is a circulating factor that reverses age-related cardiac hypertrophy. *Cell* 153, 828–839 (2013).
- Y. Y. Zhao, D. R. Sawyer, R. R. Baliga, D. J. Opel, X. Han, M. A. Marchionni, R. A. Kelly, Neuregulins promote survival and growth of cardiac myocytes. Persistence of ErbB2 and ErbB4 expression in neonatal and adult ventricular myocytes. *J. Biol. Chem.* 273, 10261–10269 (1998).
- D. Zhang, M. X. Sliwkowski, M. Mark, G. Frantz, R. Akita, Y. Sun, K. Hillan, C. Crowley, J. Brush, P. J. Godowski, Neuregulin-3 (NRG3): A novel neural tissue-enriched protein that binds and activates ErbB4. *Proc. Natl. Acad. Sci. U.S.A.* 94, 9562–9567 (1997).
- J. Li, W. Dong, X. Gao, W. Chen, C. Sun, J. Li, S. Gao, Y. Zhang, J. He, D. Lu, R. Jiang, M. Ma, X. Wang, L. Zhang, EphA4 is highly expressed in the atria of heart and its deletion leads to atrial hypertrophy and electrocardiographic abnormalities in rats. *Life Sci.* 278, 119595 (2021).
- W. Guo, D. Zhang, W. Li, Z. Zhao, B. Liu, H. Wang, F. Li, Akt-centered amplification loop plays a critical role in vascular endothelial growth factor/stromal cell-derived factor 1-α cross-talk and cardioprotection. *Chin. Med. J. (Engl)* 124, 3800–3805 (2011).
- J. Li, H. Wei, A. Chesley, C. Moon, M. Krawczyk, M. Volkova, B. Ziman, K. B. Margulies, M. Talan, M. T. Crow, K. R. Boheler, The pro-angiogenic cytokine pleiotrophin potentiates cardiomyocyte apoptosis through inhibition of endogenous AKT/PKB activity. *J. Biol. Chem.* 282, 34984–34993 (2007).
- M. Ieda, H. Kanazawa, K. Kimura, F. Hattori, Y. Ieda, M. Taniguchi, J. K. Lee, K. Matsumura, Y. Tomita, S. Miyoshi, K. Shimoda, S. Makino, M. Sano, I. Kodama, S. Ogawa, K. Fukuda, Sema3a maintains normal heart rhythm through sympathetic innervation patterning. *Nat. Med.* 13, 604–612 (2007).
- C. Delgado, L. Bu, J. Zhang, F. Liu, J. Sall, F. Liang, A. J. Furley, G. I. Fishman, Neural cell adhesion molecule is required for ventricular conduction system development. *Develop*ment 148, dev199431 (2021).

SCIENCE ADVANCES | RESEARCH ARTICLE

- A. Colliva, L. Braga, M. Giacca, S. Zacchigna, Endothelial cell-cardiomyocyte crosstalk in heart development and disease. J. Physiol. 598, 2923–2939 (2020).
- J. C. Garbern, A. Helman, R. Sereda, M. Sarikhani, A. Ahmed, G. O. Escalante, R. Ogurlu, S. L. Kim, J. F. Zimmerman, A. Cho, L. MacQueen, V. J. Bezzerides, K. K. Parker, D. A. Melton, R. T. Lee, Inhibition of mTOR signaling enhances maturation of cardiomyocytes derived from human-induced pluripotent stem cells via p53-induced quiescence. *Circulation* 141, 285–300 (2020).
- 80. T.-M. Fu, G. Hong, T. Zhou, T. G. Schuhmann, R. D. Viveros, C. M. Lieber, Stable long-term chronic brain mapping at the single-neuron level. *Nat. Methods* **13**, 875–882 (2016).
- K. Chung, J. Wallace, S.-Y. Kim, S. Kalyanasundaram, A. S. Andalman, T. J. Davidson, J. J. Mirzabekov, K. A. Zalocusky, J. Mattis, A. K. Denisin, S. Pak, H. Bernstein, C. Ramakrishnan, L. Grosenick, V. Gradinaru, K. Deisseroth, Structural and molecular interrogation of intact biological systems. *Nature* 497, 332–337 (2013).
- Y. Hao, S. Hao, E. Andersen-Nissen, W. M. Mauck III, S. Zheng, A. Butler, M. J. Lee, A. J. Wilk, C. Darby, M. Zager, P. Hoffman, M. Stoeckius, E. Papalexi, E. P. Mimitou, J. Jain, A. Srivastava, T. Stuart, L. M. Fleming, B. Yeung, A. J. Rogers, J. M. McElrath, C. A. Blish, R. Gottardo, P. Smibert, R. Satija, Integrated analysis of multimodal single-cell data. *Cell* 184, 3573–3587 e.99 (2021)
- P. Shannon, A. Markiel, O. Ozier, N. S. Baliga, J. T. Wang, D. Ramage, N. Amin, B. Schwikowski,
 T. Ideker, Cytoscape: A software environment for integrated models of biomolecular interaction networks. *Genome Res.* 13, 2498–2504 (2003).

Acknowledgments: We acknowledge C. Hartmann, N. Ramirez, and C. Gerhardinger in the Bauer Core Facility at Harvard University for assistance with sample preparation for single-cell RNA sequencing. Funding: This work was supported by the NIH (K08 HL150335 to J.C.G., HL151684 and HL137710 to R.T.L., and 1DP1DK130673 to J.L.), the National Science Foundation (NSF ECCS-2038603 to J.L. and R.T.L.), William Milton Fund (to J.L.), Harvard Stem Cell Collaborative Seed Grant (to J.L. and R.T.L.). Blavatnik Biomedical Accelerator Pilot Grant (to

R.T.L.), American Heart Association Career Development Award (to J.C.G.), Boston Children's Hospital Office of Faculty Development Career Development Award (to J.C.G.), and the Aramont Fellowship for Emerging Science Research (to J.C.G.), Author contributions: J.C.G., O.L., R.L., E.M.J., R.T.L., and J.L. designed the experimental studies, J.C.G., O.L., R.L., E.M.J., H.L.T.E., M.S., J.A., and U.-S.D. performed experimental studies and maintained iPSC cultures. R.L. prepared mesh nanoelectronics devices, characterized their performance, and recorded electrical data. Q.L. seeded cells on mesh nanoelectronics devices and recorded electrical data. Z.L. performed analysis of electrical data and scRNA-seq data. Z.L., J.C.G., R.L., and Q.L. prepared the initial draft of the manuscript and edited the manuscript, E.H. and H.S. edited the manuscript, J.C.G., R.T.L., and J.L. provided funding for personnel and experimental work. R.T.L. and J.L. supervised the research and edited the manuscript. Competing interests: R.T.L. is a cofounder, scientific advisory board member, and private equity holder of Elevian Inc. R.T.L. is a member of the scientific advisory board of Revidia Therapeutics Inc. and a consultant to BlueRock Therapeutics, J.L. is a cofounder, scientific advisory board member, and private equity holder of Axoft Inc. R.T.L., J.C.G., J.L., J.A., Q.L., and R.L. are listed as coinventors on provisional pending patent applications related to this work filed by Harvard University (filed 12 November 2021 and 11 November 2022). The authors declare that they have no other competing interests. **Data and** materials availability: Raw and processed data files for scRNA-seg were deposited to Gene Expression Omnibus [(GEO) https://www.ncbi.nlm.nih.gov/geo/] at accession number GSE210513. All data needed to evaluate the conclusions in the paper are present in the paper and/or the Supplementary Materials. The human UCSD142i-86-1 iPS cell line can be provided by WiCell pending scientific review and a completed material transfer agreement. Requests for the UCSD142i-86-1 iPS cell line should be submitted to the WiCell Research Institute.

Submitted 12 September 2022 Accepted 2 February 2023 Published 8 March 2023 10.1126/sciadv.ade8513

Downloaded from https://www.science.org at Harvard University on December 16, 2023

Science Advances

Tissue-embedded stretchable nanoelectronics reveal endothelial cell-mediated electrical maturation of human 3D cardiac microtissues

Zuwan Lin, Jessica C. Garbern, Ren Liu, Qiang Li, Estela Mancheño Juncosa, Hannah L.T. Elwell, Morgan Sokol, Junya Aoyama, Undine-Sophie Deumer, Emma Hsiao, Hao Sheng, Richard T. Lee, and Jia Liu

Sci. Adv. 9 (10), eade8513. DOI: 10.1126/sciadv.ade8513

View the article online

https://www.science.org/doi/10.1126/sciadv.ade8513

Permissions

https://www.science.org/help/reprints-and-permissions

Use of this article is subject to the Terms of service